

<sup>1</sup> Department of Physics and Electronics, CHRIST (Deemed to be University), Hosur Main Road, Bangalore, India

Abundance studies of larger flares and surges have also been carried out starting from Feldman and Widing (1990); Feldman (1992), who derived the relative abundances of elements such as Mg and O. Fludra and Schmelz (1999) derived the absolute abundances (with respect to H) of S, Ca, and Fe for 57 large flares. Similarly, Zanna and Woods (2013); Warren (2014); Sylwester *et al.* (2014); Sylwester *et al.* (2015); Dennis *et al.* (2015) used line to continuum measurements with improved spectroscopic instruments to report that the abundances of low FIP elements during the flares are near to their photospheric values. Phillips *et al.* (2003) derived the absolute abundance of K and relative abundances of Ar and S for four long-duration flares of GOES class M or higher. Narendranath *et al.* (2014) derived the absolute abundances of Fe, Ca, Si and S for 20 flares. Both Phillips *et al.* (2003) and Narendranath *et al.* (2014) found that the abundance of low FIP elements is enhanced by a factor of two in the corona while the intermediate FIP and high FIP elements retain their photospheric abundances during the flare peak. It should, however, be noted that there is a large scatter in the reported values of FIP bias from these studies due to the uncertainties arising from the different analysis techniques used (Del Zanna and Mason, 2018). Recently, inverse FIP (IFIP effect: depletion of low FIP elements in the corona with respect to the photospheric composition) was reported for Si, S and Ar during the peak of 4 X-class flares by Katsuda *et al.* (2020). Baker *et al.* (2019) had also observed the IFIP effect at the footpoints of loops during two confined M-class flares in an active region, with the flaring loop tops showing a FIP effect.

A few attempts are made to study the evolution of the abundances during large solar flares; e.g., Sylwester, Lemen, and Mewe (1984) reported spectroscopic evidence for the variation of Ca abundance during high-temperature solar flare plasmas. Narendranath *et al.* (2020) found a variation of the FIP bias during larger M class flares for the elements Fe, Ca, Si, and S. They noted that the variation is lowest for the mid-FIP element Sulfur. Further, they showed that stronger solar flares tend to have lower FIP bias.

The Solar X-ray Spectrometer (XSM) on board the Chandrayaan-2 orbiter is one of the next generation spectrometers having a higher resolution and cadence compared to earlier instruments. The XSM started solar observations in September 2019, which was during the minimum of solar cycle 24. Observations from XSM have previously been used to study the quiet Sun (Vadawale *et al.*, 2021a) and microflares (Vadawale *et al.*, 2021b) outside active regions. Mondal *et al.* (2021) derived the abundance evolution of low FIP elements - Mg, Al, Si and S during nine B-class flares. They have shown a transition of the abundances from preflare coronal to the near photospheric during the impulsive phase of the flare and again from near photospheric to the coronal values in the decay phase. To complement the XSM observations, Zanna *et al.* (2022) carried out a companion study of abundances for an active region and a B-class flare using simultaneous observations of XSM along with AIA (Lemen *et al.*, 2012) onboard Solar Dynamics Observatory (Pesnell, Thompson, and Chamberlin, 2012), as well as XRT (Golub *et al.*, 2007) and EIS (Culhane *et al.*, 2007) onboard Hinode (Kosugi *et al.*, 2007).

Though the earlier spectroscopic observations reported the variation of the abundances (or FIP bias) for the larger flares as well as smaller flares up to B-class, a detailed study for the much smaller A-class (or below) flares were difficult because of their small signals. The study of these smaller flares is of great interest in the entire solar physics community, as they are very common in active regions and may contribute to the properties of quiescent active region emission. In this work, we have used the XSM observations of much smaller flares of GOES A-class to study the elemental abundance and its evolution by performing spectroscopic analysis.

The rest of the paper is organized as follows: in Section 2 we provide details of the XSM observation, data analysis, and identification of events. In Section 3, we present the details of the spectroscopic analysis. After discussing the results in Section 4, we summarize the article in Section 5.

## 2. Observations and data analysis

The Solar X-ray Monitor (XSM: Vadawale *et al.*, 2014; Munuswamy *et al.*, 2020) on board the Chandrayaan-2 orbiter (Vanitha *et al.*, 2020) measures the Sun's disk integrated spectra from a lunar orbit, with a cadence of 1 second in the energy range of 1-15 keV (Mithun *et al.*, 2020). The unique design of XSM makes it possible to measure the X-ray intensity of the Sun over a dynamic range from below A-class to X-class activity (N P S *et al.*, 2021). It uses a Silicon Drift Detector to achieve an energy resolution better than 180 eV at 5.9 keV (Mithun *et al.*, 2020), which was the highest energy resolution broadband X-ray spectrometer observing the Sun during the minimum of solar cycle 24 covering the year 2019-2020.

During the minimum of solar cycle 24, from September 12 to November 20, 2019, and February 14 to May 19, 2020, when the Sun was in the continuous field-of-view (FOV) of XSM, it observed repeatedly flaring (GOES range of A to B class) activity within active regions. The objective of the present work is to identify all of the small A-class flares from the XSM observed light curve and then perform spectroscopic analysis to estimate the plasma parameters associated with them. A flare list of all the flares whose peak flux lies between  $10^{-8}$  to  $10^{-7} \text{ W m}^{-2}$  (in the 1-8 Å range) was compiled by visual inspection using the daily light curves available at the official website of XSM<sup>1</sup>. A total of 72 events satisfying this criterion were found.

<sup>1</sup><https://www.prl.res.in/ch2xsm/>

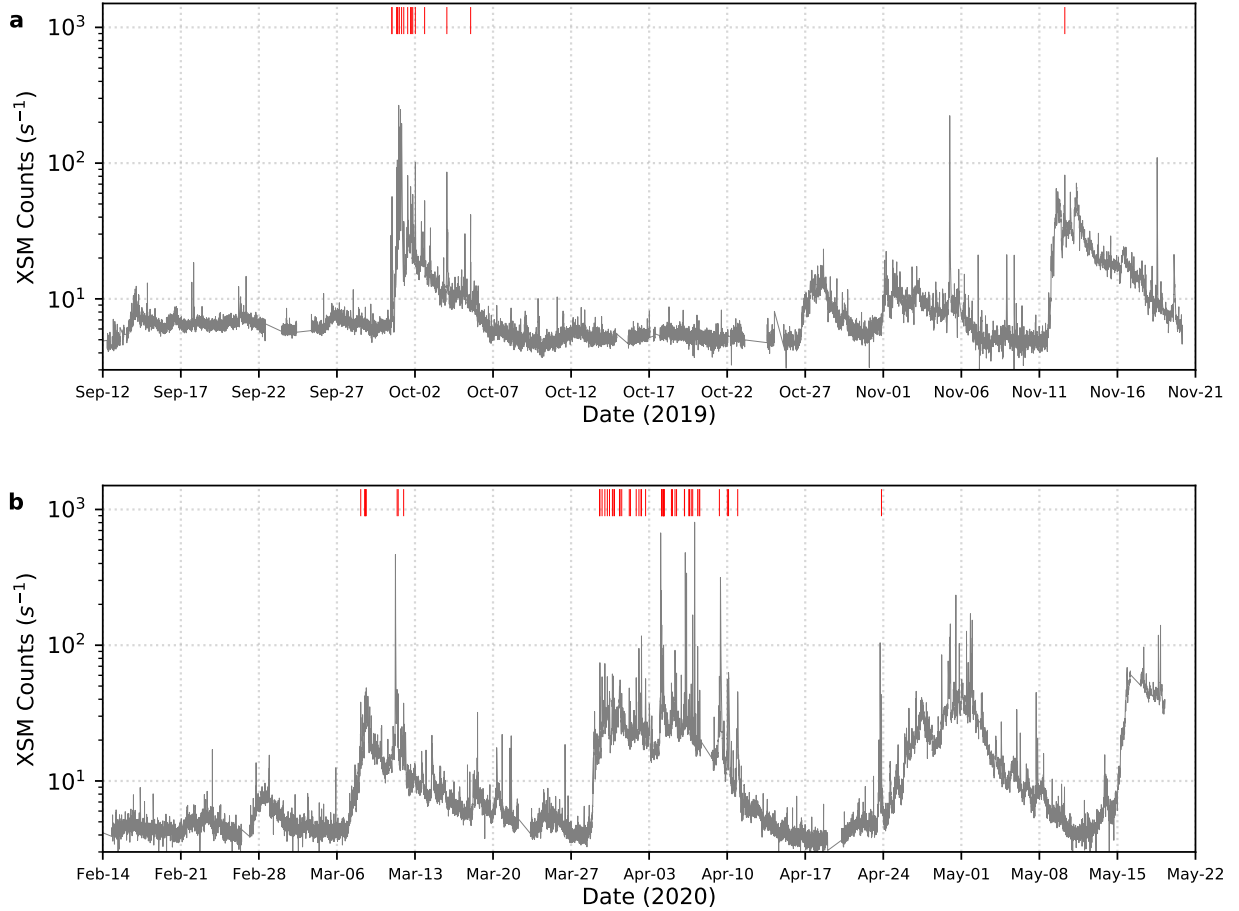


**Figure 1.** Panels **a** and **b** show the X-ray light curve in the 1-15 keV energy range with a time cadence of 120 s, as measured by XSM from September 12 to November 20, 2019, and February 14 to May 19, 2020, respectively. Vertical red lines represent the peak time of all the observed A-class flares.

XSM data used in this work is publicly available from the ISRO Space Science Data Archive (ISDA)<sup>2</sup>. XSM data consists of day-wise raw (level-1) and calibrated (level-2) files. As XSM has a wide FOV of  $\pm 40^\circ$  and it observes the Sun from a lunar orbit, there are times when the Sun is out of FOV of XSM or is occulted by the moon. Such time periods are used for generating non-solar background observations. Using the XSM level-1 data along with the XSM Data Analysis Software (XSMDAS: Mithun *et al.*, 2021), we have generated the effective area corrected XSM daily light curve in the energy range of 1-15 keV with a cadence of 120 seconds, as shown in Figure 1. All the 72 A-class flares during this period are marked by red vertical lines. From the daily light curves, the duration of A-class flares is selected for the generation of spectra as discussed in Section 3.

### 3. Spectral analysis

Soft X-ray spectrum from the Sun in the energy range of 1-15 keV contains both the continuum and line emissions. The continuum is mainly produced by free-free and free-bound emissions, with contributions also from the two-photon radiative process, whereas the line emissions primarily originate due to the atomic transitions between the different ionization states of the atoms (Del Zanna and Mason, 2018). Modelling the XSM spectrum, containing both continuum and emission lines, allows us to estimate the plasma parameters such as temperature, emission measure, and the abundances of the various elements. In this work, we have used the spectral fitting model, ‘chisoth’ (Mondal *et al.*, 2021) for the spectral analysis. ‘chisoth’ is a local model in the X-ray spectral fitting package (XSPEC: Arnaud, Dorman, and Gordon, 1999), which uses the CHIANTI database version 10 (Del Zanna *et al.*, 2021) to generate the synthetic spectra. The input parameters of this model are the logarithm of temperature, volume emission measure and the abundances of the elements with  $Z=2$  to  $Z=30$ .

We perform the time-integrated spectral analysis of all the chosen flares as described in Section 3.1. We have also performed the time-resolved spectral analysis (Section 3.2) of some of the A-class flares to understand the temporal evolution of temperature, emission measure and abundances.

<sup>2</sup><https://pradan.issdc.gov.in/pradan/>

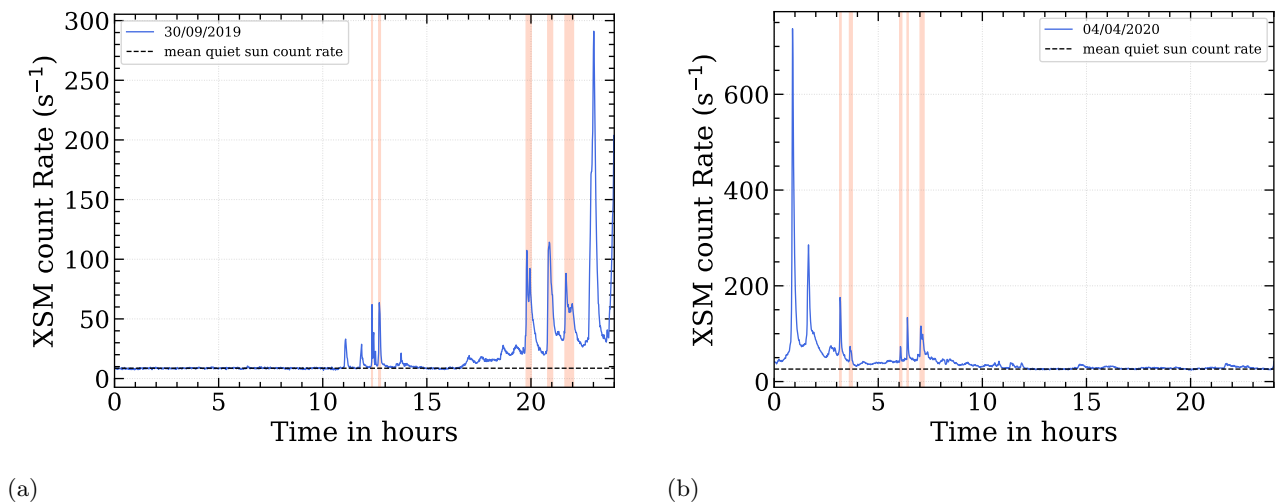


**Figure 2.** Full day XSM 1-15 keV solar X-ray light curve on 2020-09-30 (a) and 2020-04-04 (b). The red shaded regions represent the time durations used to generate the individual flaring emission spectra used for the one-temperature spectral fitting.

### 3.1. Time integrated spectral analysis

In this section, we discuss the time-integrated spectral analysis of A-class flares in the soft X-ray energy band observed by XSM. We first defined the flare start and end time when the count rate came down to 60% of the XSM peak count rate to ensure that the flaring plasma is significantly separated from the background emissions. For eight of the 72 flares observed, the background active region emission is found to be more than 60% of the peak rate. Thus, excluding these, the remaining 65 flares are selected for further analysis. Time-integrated spectrum, along with the corresponding Ancillary Response File (ARF), for the selected duration was generated using the ‘xsmgenspec’ module of the XSMDSAS by selecting the Good Time Intervals (GTI). Figure 2 shows the light curves for two representative days of 2019-09-30 (panel a) and 2020-04-04 (panel b) where the red-shaded regions represent durations of the A-class flares for which the time-integrated spectra is generated.

For the analysis of the flare spectra, the energy range of below 1.3 keV is ignored due to the uncertainty of XSM response to these low energies (Mithun *et al.*, 2021). The higher energy is also limited to where the solar X-ray spectrum dominates over the non-solar background. The modelling of the spectra is carried out by assuming that the emission is coming from plasma at a single-temperature, as shown in Figure 3 for two representative flares, where the grey points show the background spectra. The abundances of Mg, Al, Si and S (in most cases), whose emission complexes are visible clearly, along with temperature and emission measure are kept as free parameters. All other elemental abundances are frozen to their coronal values taken from Schmelz *et al.* (2012). The best-fitted parameters for all the flares, along with the one sigma uncertainties estimated using the standard procedure in XSPEC, are given in Table 1. The same results are plotted against the flare number (flare numbers are IDs given to the flares according to their flare sub-class in ascending order) in Figure 4. For comparison, we have carried out the time-integrated analysis of the 9 B-class flares studied in Mondal *et al.* (2021) and plotted the plasma parameters in the same figure (Figure 4).

### 3.2. Time resolved spectral analysis

We have carried out the time-integrated spectral analysis of all the chosen flares as discussed in Section 3.1. However, carrying out the time-resolved spectroscopy for these individual flares is challenging due to their weak signals. In order to increase the signal-to-noise ratio of these small flares, we have added the spectra of multiple flares having similar rise time, peak counts, and decay time. Figure 6 shows the rise time (RT: Panel a), the peak count rate (PCR: Panel b) and the decay time (DT: Panel c) of all the flares. We have identified flares having approximately equal values of RT, PCR, and DT. The selected sets of flares were over-plotted by co-aligning the flare peak at zero seconds. Further, by visual inspection, we kept only those flares in a set which followed a similar evolutionary profile. This selection resulted in seven sets of near-identical flares. All the flares of a particular set are marked with arrows of the same colour (set 1 - blue, set 2 - brown, set 3 - red, set 4 - grey, set 5 - orange, set 6 - black, set 7 - green in Figure 6). The properties of all the flares considered in each set are given in Table 1. The over-plotted light curves of three representative sets (set 1, set 2 and set 3) of flares out of the seven are shown in panels a-c of Figure 7. Panel a contains a set of two A3-class flares, Panel b contains a set of two flares of class A2.6 and A2.7 and Panel c contains a set of three A1.2-class flares. As A1-class flares are very weak, three flares are required in this set in order to constrain the spectral parameters. We have divided these sets of flares into multiple time bins, as shown by the alternative orange and grey shaded regions.

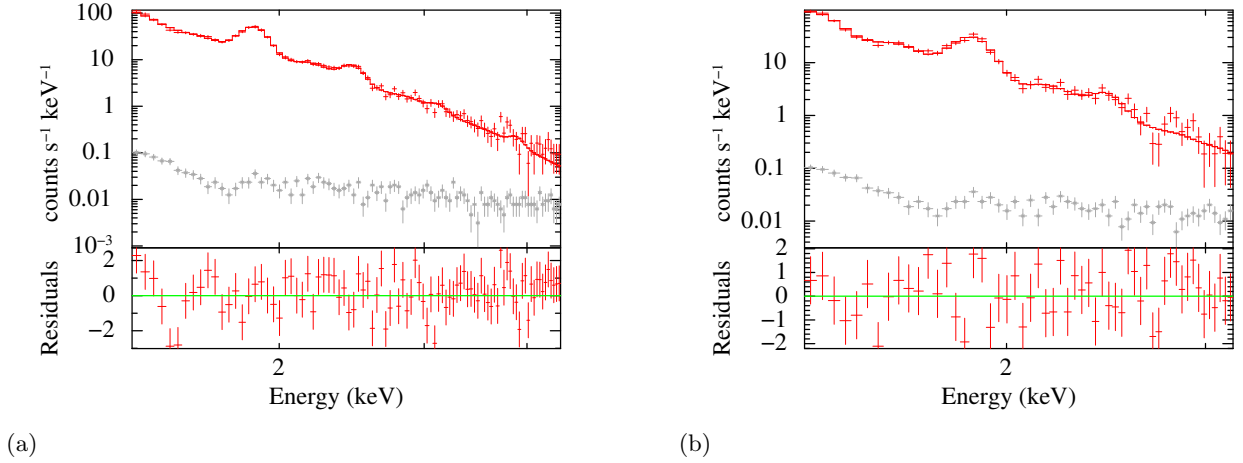


**Figure 3.** Fitted 1T-spectrum (red) for the Flare SOL20190930T19:47 (a) and SOL20200404T06:03 (b). The grey points represent the non-solar background spectrum generated for the times when the Sun was out of the FOV of XSM. The spectral fits' energy ranges were limited to those where the solar X-ray spectrum dominates over the non-solar background.

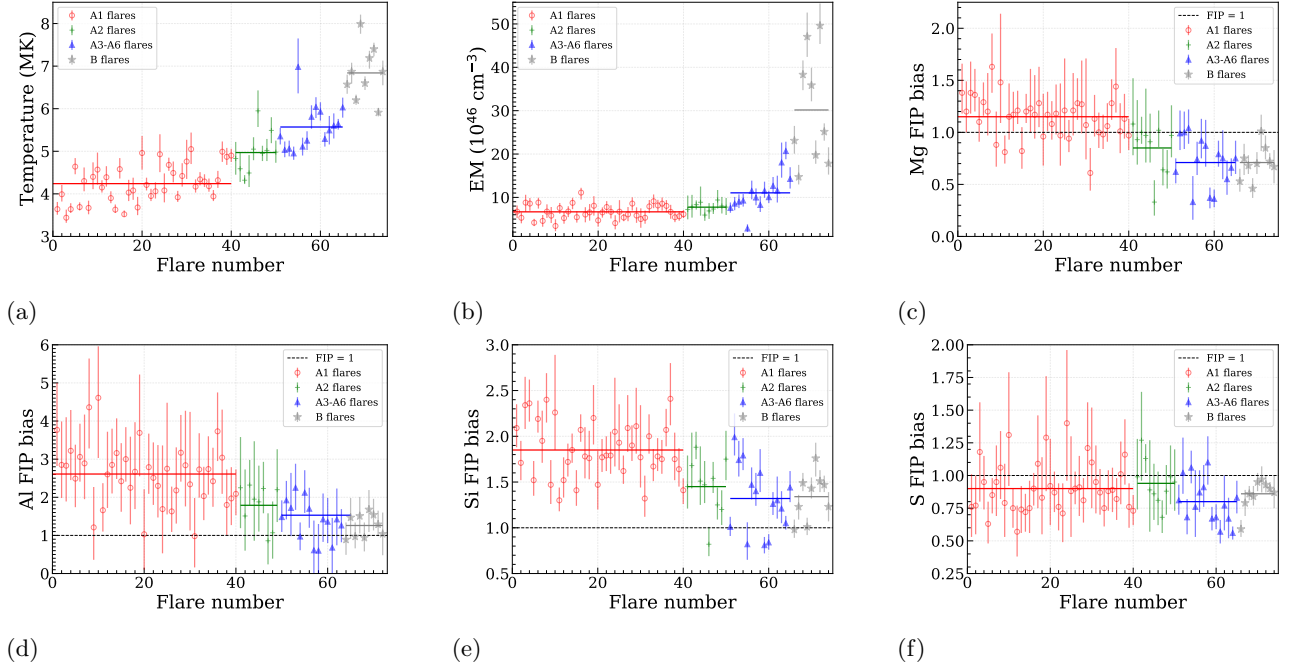


**Figure 4.** Results from the 1T time-integrated spectral analysis for all the 65 A-class flares considered in this study and 9 B-class flares studied in Mondal *et al.* (2021). Panels **a** and **b** show the temperature and emission measure values. Panels **c-f** show the values of FIP bias of Mg, Al, Si and S, respectively. Red circles represent A1 flares, green cross represents A2 flares, blue triangles represent A3-A6 flares, and grey stars represent B-class flares. The horizontal lines represent the average parameter values of each sub-class. The horizontal black dashed line marks a FIP bias of 1 in panels **c-f**.

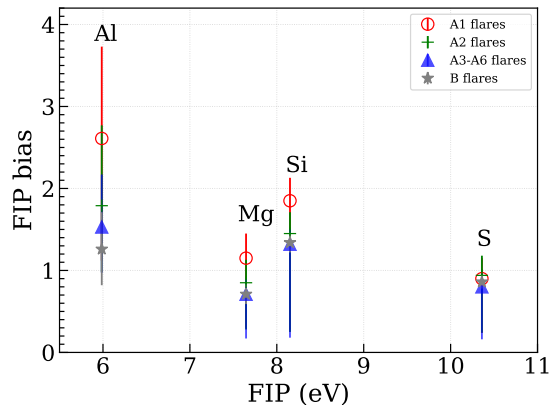


**Figure 5.** Average FIP bias values of A1, A2, A3-A6 flares (red circles, green cross, blue triangles respectively: this study), B-class flares (grey stars: Mondal *et al.*, 2021) plotted against the first ionization potential.

**Table 1.** Flare properties of all the flares considered in each set of similar flares. Flare IDs corresponding to peak times of the flares is given in the format SOLyyyy-mm-ddThh:mm. Approximate GOES classes are mentioned according to the peak flux of the flare in the 1-8 Å XSM flux. Peak count rate, rise time and decay time are calculated from the XSM light curve.

Set number	Flare IDs	Flare class	Peak count rate ( $\text{s}^{-1}$ )	Rise time (Hours)	Decay time (Hours)
Set 1	SOL2019-10-04T01:00	A3.0	92.4	0.45	0.13
	SOL2020-04-05T07:42	A3.0	98.83	0.48	0.16
Set 2	SOL2020-03-29T14:02	A2.7	83.83	0.01	0.05
	SOL2020-03-30T00:40	A2.6	80.31	0.03	0.05
Set 3	SOL2020-03-31T13:01	A1.2	49.05	0.04	0.14
	SOL2020-04-02T06:31	A1.2	50.19	0.07	0.12
	SOL2020-03-29T13:16	A1.2	47.52	0.04	0.17
Set 4	SOL2020-04-10T00:22	A1.8	61.23	0.03	0.12
	SOL2019-10-01T20:33	A1.9	65.1	0.02	0.18
Set 5	SOL2020-04-07T11:36	A1.1	44.7	0.07	0.07
	SOL2020-03-08T03:15	A1.2	43.06	0.05	0.08
	SOL2020-03-11T11:50	A1.3	48.6	0.02	0.08
Set 6	SOL2020-04-04T03:38	A2.0	73.15	0.01	0.07
	SOL2020-04-09T07:14	A2.0	68.72	0.02	0.06
Set 7	SOL2020-04-02T02:04	A3.1	109.9	0.03	0.07
	SOL2019-10-02T00:33	A3.4	110.3	0.04	0.08

Spectra is generated for each of these time bins, for all the flares of a set, in a similar way as discussed in Section 3.1. The spectra of corresponding bins of all the flares in a set are added using the ‘xsmaddspec’ module of XSM DAS. The spectral analysis for each added spectra is carried out (Section 3.1) using the 1T ‘chisoth’ model by keeping the temperature, emission measure and abundances of Mg, Al, and Si as free variables. The abundance of S was kept free only for selected time bins of set 1 of flares (two A3-class flares) as it was not possible to constrain its value in other sets due to poor statistics. The obtained best-fit parameters with the one sigma errors are plotted in Figure 8 for the three representative sets of flares. The evolution of temperature (Figure 9), emission measure (Figure 10) and abundances (Magnesium : Figure 11, Aluminium: Figure 12, Silicon: Figure 13, Sulfur: Figure 14) for all the other sets of flares is shown in the Appendix.

#### 4. Results and discussion

In this work, we have studied 65 A-class flares that were observed by XSM during the minimum of solar cycle 24. Analyzing the broadband spectra observed by XSM during these flares, we have derived the average plasma parameters (i.e., temperature, emission measure, and the abundances of low FIP elements Mg, Al, Si, and S). The results are shown in Figure 4, and the same is tabulated in the Appendix (Table 2). The different panels in Figure 4 represent the variation of temperature (a), emission measure (b), FIP bias of Mg (c), Al (d), Si (e), and S (f) with the flare number. The points with error bars in each panel represent the plasma parameters associated with each flare. The flares are grouped according to their sub-class, and the associated parameters of each group are shown by the same colour; e.g., the A1 class flares are shown by red error bars, whereas the A2 class flares are shown by green error bars, and so on. The horizontal line associated with each group represents the average value for all the flares in that group. The results show that the temperature and emission measure of

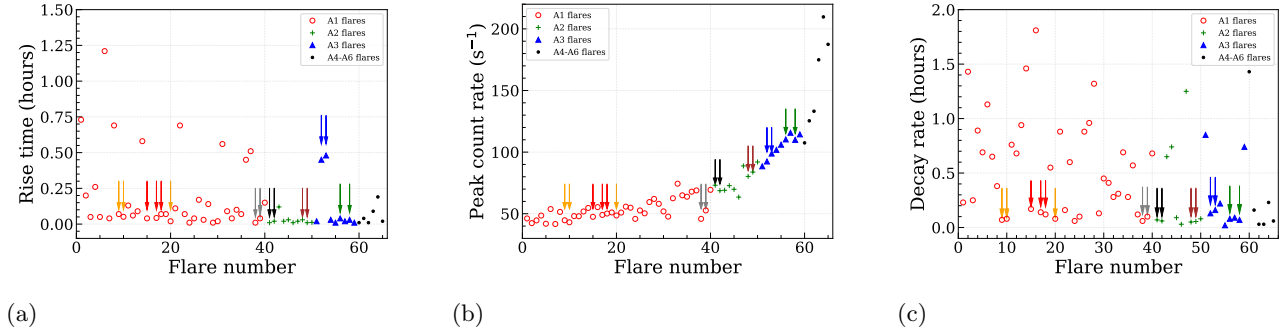


**Figure 6.** Panels **a**, **b** and **c** show the peak count rate, rise time and decay time (in hours) versus flare number for all the 65 flares considered in this study. Seven sets of flares having similar values in all three plots, as well as similar flaring light curves, are selected for performing time-resolved spectral analysis as described in Section 3.2. All the flares of a set are marked with arrows of the same colour (set 1 - blue, set 2 - brown, set 3 - red, set 4 - grey, set 5 - orange, set 6 - black, set 7 - green).

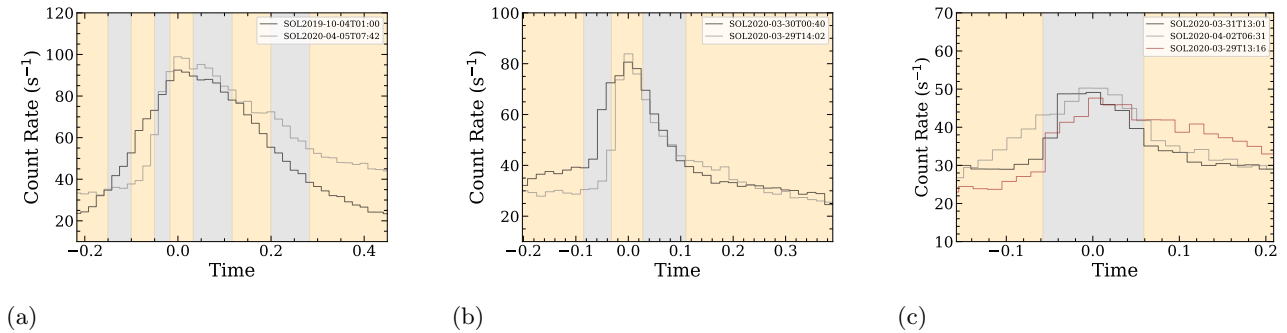


**Figure 7.** The 1-15 keV XSM X-ray light curves for three representative sets (set 1, set 2 and set 3) of flares. Background orange and grey shaded regions demarcate durations for which the integrated XSM spectra have been generated for each of the flares in a set and then added to carry out the time-resolved spectroscopy as described in Section 4. The flare IDs for all the flares of a set are given in the legend in the format SOLyyyy-mm-ddThh:mm.

the flaring plasma varies and scales with the flare sub-class, whereas the FIP bias of Mg, Al, Si, and S does not show a similar variation. The flares-groups with lower activity (e.g., A1 class) are found to have intermediate FIP bias (specifically for Si and Al), whereas the higher class of flare-groups (e.g., A3-A6 class) have a lower FIP bias. For comparison purposes, we also have shown the average plasma parameters for the higher B-class flares, which are observed by XSM and studied in detail by Mondal *et al.* (2021).

Earlier studies during the peak of larger solar flares have found that the FIP bias is close to unity (e.g., Warren, 2014; Narendranath *et al.*, 2014; Dennis *et al.*, 2015; Sylwester *et al.*, 2015), which indicates that unfractionated plasma materials from the lower solar atmosphere (e.g., beneath the chromosphere) evaporates through the flaring loops during the flaring process (Benz, 2017). In the present analysis, a near unity FIP bias for the integrated duration of the larger flares indicates the same phenomenon of evaporation of the unfractionated plasma. During these flares, the emission from the hot ( $> 3$  MK) evaporated plasma is dominated over the surrounding quiescent AR emission of temperature  $\sim 3$  MK (Figure 4a and Figure 4b). If the evaporation of the plasma from the depth of the lower atmosphere is a common phenomenon for the large as well as for the small flares, the flaring plasma should have a FIP bias of one. But the smaller flares show intermediate FIP bias (specifically for Si and Al, as shown in Figure 4). Several factors could account for these findings. First, and most likely, the enormous emission from the surrounding AR plasma (having higher FIP bias) is mixed with the smaller emission of the evaporated plasma (having unit FIP bias) from these tiny flares. The second possibility is that the plasma is being fractionated (i.e., ions are separating from neutrals) from a layer that is much lower than the layer from which the plasma is evaporating. To understand this further, we have carried out the time-resolved spectroscopic study of these small flares, as discussed later.

We also note that the FIP bias deviation between the smaller and larger class of flares is not the same for all the elements. Figure 5 shows the variation of average FIP bias of the elements for each flare group with the FIP values. The deviation is more for Al, which has the lowest FIP value among the four elements considered in this study, while the FIP bias deviation is the smallest for S, which has the highest FIP value. S is considered as an intermediate FIP element (Feldman, 1992). Thus, its FIP bias is intrinsically small for the coronal plasma (Sylwester *et al.*, 2012), which explains our results of similar FIP bias of S for all the flare groups.

In addition to the time-integrated study of the A-class flares, it is interesting to see the evolution of the plasma parameters during these flares using the time-resolved spectroscopic analysis. However, poor statistics of the observed spectra from these small flares restrict the performance of the time-resolved spectroscopic analysis. Thus, in order to carry out the time-resolved spectral analysis, we have chosen multiple A-class flares having

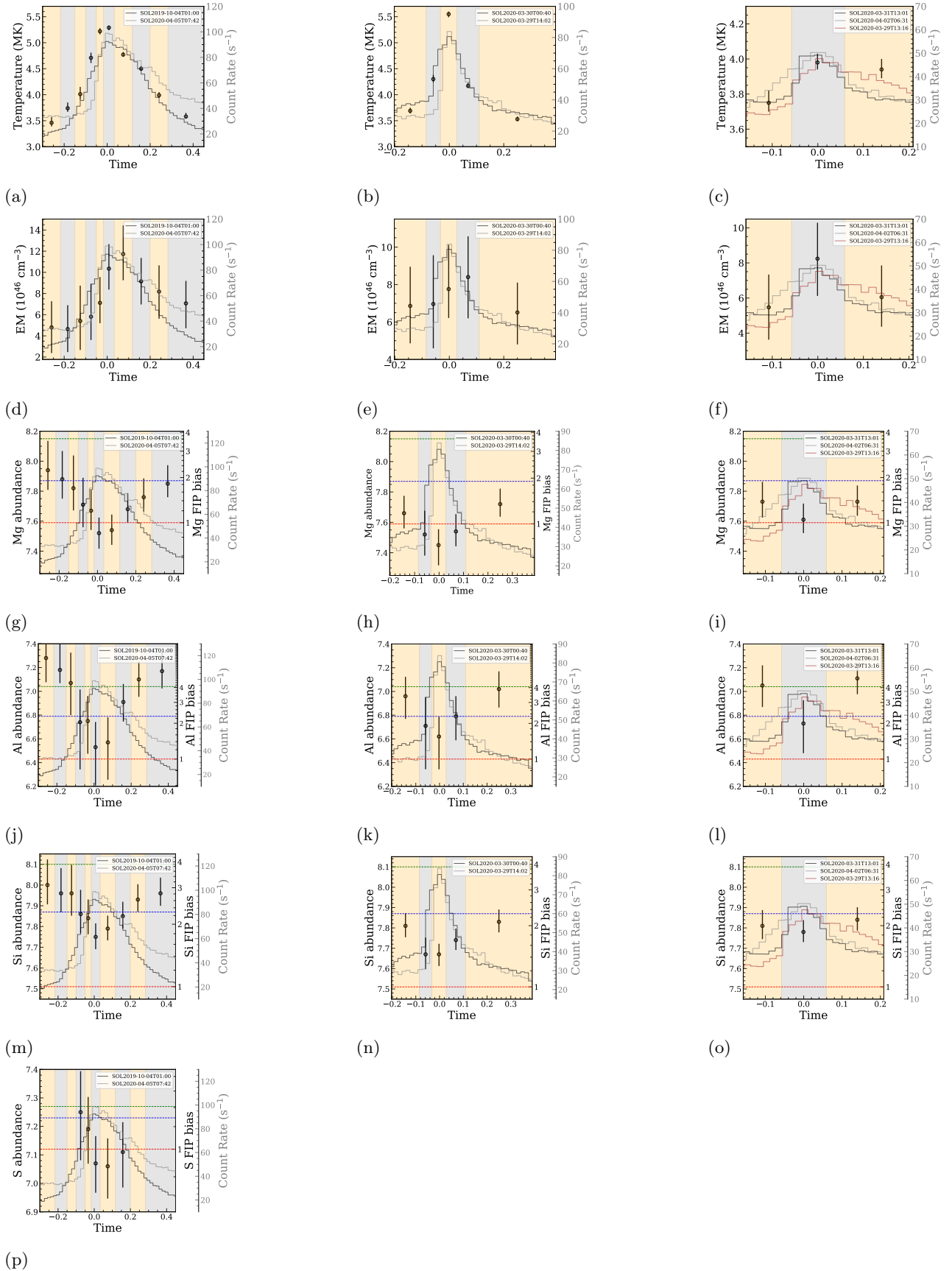


**Figure 8.** The above panels show the results of the time-resolved X-ray spectroscopy for three representative sets of flares (set 1, set 2 and set 3). Panels a-c and d-f show the variation of temperature and emission measure. Panels g-i, j-l, m-o and p show the variation of elemental abundances of Mg, Al, Si and S in logarithmic scale. In panels g-p, the red horizontal dotted line represents the photospheric abundances from Asplund *et al.* (2009) and the blue and green horizontal line represents the coronal abundances from Schmelz *et al.* (2012) and Feldman (1992) respectively. The X-ray XSM light curves of all the flares of a set are over-plotted in grey (only in Panels a,d,g,j and m) in the background.



similar rise times, peak counts, and decay times (Figure 6). After co-aligning all of these similar flares with respect to their peak time, we have added their spectra to increase the counting statistics. We perform the time-resolved spectroscopy of the added spectra and estimate the temporal evolution of the plasma parameters as stated in Section 3.2. Here, we assume that the emission mechanism of the flaring plasmas with respect to the peak time is similar for all of these flares, which is a valid assumption for all the flares having similar X-ray light curves. Results for three representative sets of flares are shown in Figure 8. The panels **a-c** show the evolution of temperature, **d-f** show the evolution of emission measure, panels **g-i**, **j-l**, **m-o** show the evolution of the abundances of Mg, Al, Si respectively. Panel **p** shows the evolution of the S abundance during the peak of set 1 when the signal at the energy of the S line complex is good enough to constrain its abundance in the spectral fitting. In the background, the light curves of the flares are shown by solid grey lines. We find that both the temperature and emission measure follow the X-ray light curve of the flares with a maximum near the peak. During the impulsive phase, the abundances of the elements reduce from the coronal values (as shown by dashed green and blue lines taken from Feldman (1992) and Schmelz *et al.* (2012) respectively) towards the photospheric values (red dashed line: Asplund *et al.* (2009)) and reach their minima during the flare peak. The elemental abundances quickly return to their preflare coronal values during the decay phase. From our observations, we find that the recovery rate of the coronal FIP bias is of the order of minutes. Typically, it varies between  $\sim 4$  to  $\sim 10$  minutes. The evolution of parameters is similar to that seen for the larger B-class of flares as reported by Mondal *et al.* (2021).

The evolution of temperature and emission measures can be explained using the standard flare model (CSHKP: Carmichael, 1964; Sturrock, 1966; Hirayama, 1974; Kopp and Pneuman, 1976). Once the flaring mechanism is initiated by the process of reconnection, heat energy from the reconnection site flows down to the chromosphere and begins rapidly evaporating the chromospheric plasma into the loop with high velocity (Antonucci *et al.*, 1985). The hot and dense chromospheric plasma fills the flaring loop, causing an increase in temperature and emission measures. The temperature and emission measure reaches its peak when the loop is mostly filled with high-density heated evaporated material (Ryan *et al.*, 2012; Klimchuk, 2017). The rapid depletion of abundance can be explained by the evaporative up-flow, which transports unfractionated chromospheric material into the corona. However, the rapid recovery (in a time frame of minutes) of the coronal FIP bias during the flare decay stages is challenging to explain.

The Ponderomotive force model (Laming, 2004; Laming and Hwang, 2009; Laming, 2012; Laming, 2015) is the widely accepted explanation of the FIP effect in closed-loop coronal structures (e.g., active regions). In closed loops, this model suggests that downward propagating coronal Alfvén waves, which could be generated by coronal nanoflares (Dahlburg *et al.*, 2016), can reflect from the chromospheric heights and generate Ponderomotive force. This force is directed upwards and acts only on the ions (not the neutrals) present in the chromospheric layers, causing a fractionation of the ions and the neutrals within the local plasma. The temperature and the density of the chromospheric plasma are such that only the low FIP elements are ionized and are present at the fractionation region, and thus the Ponderomotive force acts only on the ions of low FIP elements. The local fractionation of the plasma at the chromospheric height can produce the FIP bias in a short time scale of a few minutes ( $\sim 10$  min) (Baker *et al.*, 2015). Once the fractionation occurs, the chromospheric fractionated plasma reaches the corona by the process of transportation or diffusion. Widing and Feldman (2001) observationally measured that the FIP bias within the newly emerging AR loops is developed in a time scale of days, which is close to the diffusion time scale. In the present study, during the decay phase of the A-class flares, we find the coronal FIP bias is developed on a time scale of a few minutes ( $\sim 4$  min to 10 min). This is possible by quickly transporting the fractionated chromospheric plasma to the corona or/and by increasing the fractionation rate of the chromospheric plasma. For these, Mondal *et al.* (2021) suggested two possible scenarios. One is based on the evaporation process during the flare, which can transport the chromospheric fractionated plasma very quickly to the corona in the decay phase of the flares. The other scenario is based on the evaporation process as well as the flare-driven Alfvén waves. In the decay phase, the reflection of the high amplitude flare-driven Alfvén waves fractionates the chromospheric plasma at a much faster rate, and then this fractionated plasma is evaporated to the corona, causing a rapid development of the coronal FIP bias.

As the FIP build-up in the decay phase of the few flares is happening in a few minutes time scale, we prefer the second scenario of Mondal *et al.* (2021), which relies on the evaporation velocity as well as the flare-driven Alfvén waves. In this case to explain both the depletion and recovery of the FIP bias during the impulsive and decay phases, the heat transported from the flaring site at the corona should be faster than the flare-driven Alfvén waves. This could be possible by transporting the heat by the suprathermal electrons, which is known to have a faster speed than the Alfvén speed (Benz, 2017). Just after the initiation of the flare by the onset of the reconnection, heat is quickly transported to the chromosphere and starts rapid evaporation causing a depletion of the abundance until flare-peak. In the decay phase, high amplitude flare-driven Alfvén waves reach the chromosphere and fractionate the plasma at a faster rate. This fractionated plasma is carried by the evaporation processes to develop the coronal FIP bias at a faster rate. It is to be noted that the flare-driven Alfvén waves are yet to be observed in the solar corona with our present generation instrumentation and techniques. However, our results indicate their existence even during the small A-class flares. To increase our understanding of this topic, a detailed simulation/modeling effort is needed further.

## 5. Summary

We report the X-ray spectroscopic measurements of the plasma temperature, emission measure, and elemental (Mg, Al, Si, and S) abundances for a large number of A-class flares observed by XSM/Chandrayaan-2 during the minimum of solar cycle 24. Time-integrated spectral analysis during these flares shows that the average temperature and emission measure scales with the flare sub-class, whereas the FIP bias of the elements does not follow the same behavior. The higher A-class flares show a FIP bias of near unity, indicating the evaporation of the un-fractionated plasma materials from the lower solar atmosphere to the corona, while the lower A-class flares show an intermediate FIP bias, either due to the mixing-up of background solar emissions with the small flaring emissions, or/and the evaporated plasma materials are already fractionated. We have also derived the time evolution of the parameters using the time-resolved spectroscopic analysis. Due to the small emissions from these flares, it is challenging to carry out time-resolved spectroscopy using the sun-as-a-star observation of XSM. Thus, we have added the observed spectrum of multiple flares with similar properties (similar flare class, rise and decay times). We find that during the impulsive phase, the temperature and emission measure increases, while the elemental abundances drop towards photospheric values and reach a minimum near the peak. In the decay phase, the abundances are seen to quickly return to their coronal values on a time scale of minutes, similar to the higher B-class flares, as reported earlier. These observations suggest the existence and role of flare-driven Alfvén waves in increasing the fractionation rate and transporting the fractionated plasma to the corona through the evaporation processes, even in A-class flares. Further simulations and the spectroscopic measurements of smaller flares with future instrumentation will help to increase our understanding of the topic.

**Acknowledgments** XSM was designed and developed by the Physical Research Laboratory (PRL), Ahmedabad, with support from the Space Application Centre(SAC), Ahmedabad, the U. R. Rao Satellite Centre (URSC), Bengaluru, and the Laboratory for Electro-Optics Systems (LEOS), Bengaluru. We thank various facilities and the technical teams of all the above centers and the Chandrayaan-2 project, mission operations, and ground segment teams for their support. The Chandrayaan-2 mission is funded and managed by the Indian Space Research Organisation (ISRO). We are very grateful to Mithun N.P.S and Dr. Santosh Vadawale for the helpful scientific discussions and important suggestions for this work. I acknowledge the support and resources provided during my visit to Physical Research Laboratory (PRL), Ahmedabad, thanks to Dr. Anil Bhardwaj.

## Appendix

**Table 2.:** Plasma parameters obtained from the 1T spectral analysis for all the A-class flares considered in this study. Flare IDs corresponding to peak times of the flares is given in the format SOLyyy-mm-ddThh:mm. Approximate GOES classes are mentioned according to the peak flux of the flare in the 1-8 Å XSM flux. Errors correspond to the  $1\sigma$  limits associated with the parameters.

Sl no	Flare ID	Flare Class (GOES approximation)	Temperature (MK)	Emission Measure ( $\times 10^{46} \text{cm}^{-3}$ )	Mg FIP bias	Al FIP bias	Si FIP bias	S FIP bias
1	SOL2019-09-30T12:21	A3.3	$6.98^{+0.67}_{-0.62}$	$2.83^{+0.97}_{-0.79}$	$1.38^{+0.28}_{-0.20}$	$3.77^{+1.23}_{-0.95}$	$2.09^{+0.26}_{-0.21}$	$0.76^{+1.01}_{-0.53}$
2	SOL2019-09-30T12:42	A2.3	$5.95^{+0.48}_{-0.38}$	$6.88^{+1.81}_{-1.84}$	$1.20^{+0.29}_{-0.20}$	$2.85^{+1.14}_{-0.87}$	$1.71^{+0.24}_{-0.19}$	$0.77^{+1.00}_{-0.55}$
3	SOL2019-09-30T19:47	A4.1	$5.93^{+0.22}_{-0.21}$	$10.05^{+1.50}_{-1.35}$	$1.38^{+0.30}_{-0.20}$	$2.83^{+1.27}_{-0.94}$	$2.34^{+0.31}_{-0.26}$	$1.18^{+1.56}_{-0.80}$
4	SOL2019-09-30T20:49	A3.9	$6.04^{+0.23}_{-0.26}$	$11.52^{+2.11}_{-1.59}$	$1.36^{+0.25}_{-0.16}$	$3.22^{+1.07}_{-0.77}$	$2.36^{+0.26}_{-0.20}$	$0.95^{+1.15}_{-0.74}$
5	SOL2019-09-30T21:40	A3.0	$5.35^{+0.20}_{-0.19}$	$7.57^{+1.26}_{-1.11}$	$1.10^{+0.24}_{-0.19}$	$2.49^{+0.89}_{-0.75}$	$1.52^{+0.21}_{-0.17}$	$0.63^{+0.80}_{-0.48}$
6	SOL2019-10-01T03:26	A6.4	$5.64^{+0.12}_{-0.13}$	$20.69^{+2.15}_{-1.89}$	$1.29^{+0.19}_{-0.13}$	$3.06^{+0.87}_{-0.65}$	$2.19^{+0.20}_{-0.15}$	$0.85^{+0.98}_{-0.72}$
7	SOL2019-10-01T06:45	A1.1	$4.64^{+0.20}_{-0.18}$	$4.18^{+0.88}_{-0.80}$	$1.20^{+0.37}_{-0.23}$	$2.89^{+1.28}_{-0.94}$	$1.95^{+0.33}_{-0.24}$	$0.95^{+1.23}_{-0.70}$
8	SOL2019-10-01T12:47	A2.6	$4.95^{+0.18}_{-0.18}$	$7.32^{+1.39}_{-1.14}$	$1.63^{+0.32}_{-0.25}$	$4.36^{+1.28}_{-1.08}$	$2.40^{+0.29}_{-0.25}$	$1.06^{+1.34}_{-0.82}$
9	SOL2019-10-01T17:14	A1.7	$4.34^{+0.17}_{-0.14}$	$9.11^{+1.57}_{-1.60}$	$0.88^{+0.32}_{-0.21}$	$1.21^{+1.06}_{-0.85}$	$1.47^{+0.27}_{-0.21}$	$0.79^{+1.09}_{-0.53}$
10	SOL2019-10-01T18:55	A1.4	$4.06^{+0.21}_{-0.17}$	$6.67^{+1.52}_{-1.53}$	$1.48^{+0.66}_{-0.39}$	$4.61^{+2.35}_{-1.58}$	$2.26^{+0.63}_{-0.41}$	$1.31^{+1.79}_{-0.92}$
11	SOL2019-10-01T20:33	A1.9	$4.87^{+0.21}_{-0.19}$	$5.65^{+1.17}_{-1.04}$	$0.81^{+0.16}_{-0.11}$	$1.66^{+0.71}_{-0.56}$	$1.30^{+0.14}_{-0.12}$	$0.75^{+0.90}_{-0.60}$
12	SOL2019-10-02T00:33	A3.4	$5.11^{+0.21}_{-0.21}$	$11.50^{+2.37}_{-1.96}$	$1.15^{+0.32}_{-0.22}$	$2.60^{+1.12}_{-0.88}$	$1.52^{+0.25}_{-0.19}$	$0.57^{+0.77}_{-0.38}$
13	SOL2019-10-02T14:49	A1.5	$4.49^{+0.27}_{-0.22}$	$6.09^{+1.69}_{-1.58}$	$1.17^{+0.22}_{-0.16}$	$2.85^{+0.95}_{-0.75}$	$1.72^{+0.20}_{-0.16}$	$0.74^{+0.92}_{-0.57}$
14	SOL2019-10-04T01:00	A3.0	$5.03^{+0.20}_{-0.17}$	$8.57^{+1.54}_{-1.53}$	$1.21^{+0.19}_{-0.13}$	$3.16^{+0.91}_{-0.68}$	$1.85^{+0.18}_{-0.14}$	$0.72^{+0.87}_{-0.57}$
15	SOL2019-10-05T13:34	A1.4	$4.93^{+0.47}_{-0.42}$	$4.07^{+1.82}_{-1.44}$	$0.82^{+0.23}_{-0.17}$	$2.42^{+1.00}_{-0.80}$	$1.41^{+0.22}_{-0.17}$	$0.75^{+0.96}_{-0.56}$
16	SOL2019-11-12T15:06	A2.9	$4.98^{+0.27}_{-0.25}$	$7.76^{+2.10}_{-1.81}$	$1.20^{+0.17}_{-0.11}$	$3.00^{+0.84}_{-0.59}$	$2.07^{+0.17}_{-0.13}$	$0.90^{+1.01}_{-0.76}$
17	SOL2020-03-08T03:15	A1.2	$4.57^{+0.40}_{-0.35}$	$3.41^{+1.55}_{-1.21}$	$1.23^{+0.38}_{-0.23}$	$2.25^{+1.34}_{-0.96}$	$1.78^{+0.32}_{-0.24}$	$1.09^{+1.46}_{-0.75}$

Sl no	Flare ID	Flare Class (GOES approximation)	Temperature (MK)	Emission Measure ( $\times 10^{46} \text{cm}^{-3}$ )	Mg FIP bias	Al FIP bias	Si FIP bias	S FIP bias
18	SOL2020-03-08T11:47	A1.2	$4.15^{+0.17}_{-0.12}$	$7.54^{+1.18}_{-1.31}$	$1.17^{+0.35}_{-0.23}$	$2.67^{+1.30}_{-0.98}$	$1.76^{+0.30}_{-0.23}$	$0.83^{+1.14}_{-0.55}$
19	SOL2020-03-08T12:42	A1.2	$4.39^{+0.26}_{-0.22}$	$5.23^{+1.42}_{-1.30}$	$1.28^{+0.35}_{-0.23}$	$3.69^{+1.53}_{-1.14}$	$2.20^{+0.36}_{-0.29}$	$1.29^{+1.76}_{-0.87}$
20	SOL2020-03-08T13:19	A1.2	$3.90^{+0.16}_{-0.12}$	$6.75^{+1.21}_{-1.30}$	$0.96^{+0.41}_{-0.28}$	$1.03^{+1.18}_{-0.93}$	$1.47^{+0.37}_{-0.27}$	$0.92^{+1.28}_{-0.62}$
21	SOL2020-03-08T15:11	A1.2	$3.63^{+0.12}_{-0.08}$	$8.75^{+1.18}_{-1.47}$	$1.17^{+0.22}_{-0.16}$	$2.79^{+0.88}_{-0.70}$	$1.77^{+0.20}_{-0.16}$	$0.87^{+1.03}_{-0.72}$
22	SOL2020-03-11T09:36	A1.1	$3.69^{+0.11}_{-0.08}$	$8.81^{+1.12}_{-1.39}$	$1.08^{+0.22}_{-0.15}$	$2.51^{+0.93}_{-0.71}$	$1.79^{+0.21}_{-0.17}$	$0.76^{+0.94}_{-0.59}$
23	SOL2020-03-11T11:50	A1.3	$4.96^{+0.40}_{-0.39}$	$4.70^{+1.95}_{-1.43}$	$1.18^{+0.28}_{-0.20}$	$2.30^{+1.07}_{-0.83}$	$1.79^{+0.26}_{-0.20}$	$0.71^{+0.94}_{-0.49}$
24	SOL2020-03-11T23:35	A1.1	$4.30^{+0.32}_{-0.24}$	$4.58^{+1.36}_{-1.34}$	$0.97^{+0.50}_{-0.29}$	$1.69^{+1.67}_{-1.16}$	$2.05^{+0.59}_{-0.38}$	$1.40^{+1.96}_{-0.96}$
25	SOL2020-03-29T13:16	A1.2	$4.58^{+0.26}_{-0.22}$	$5.43^{+1.37}_{-1.24}$	$1.21^{+0.50}_{-0.28}$	$2.75^{+1.73}_{-1.20}$	$1.93^{+0.42}_{-0.30}$	$0.88^{+1.30}_{-0.53}$
26	SOL2020-03-29T14:02	A2.7	$5.49^{+0.31}_{-0.30}$	$8.02^{+2.09}_{-1.73}$	$0.94^{+0.18}_{-0.13}$	$1.63^{+0.65}_{-0.54}$	$1.62^{+0.17}_{-0.14}$	$0.90^{+1.03}_{-0.78}$
27	SOL2020-03-29T18:43	A1.7	$4.29^{+0.17}_{-0.13}$	$8.14^{+1.31}_{-1.45}$	$1.21^{+0.36}_{-0.24}$	$2.18^{+1.13}_{-0.87}$	$2.09^{+0.36}_{-0.26}$	$0.91^{+1.16}_{-0.69}$
28	SOL2020-03-30T00:44	A2.6	$5.02^{+0.27}_{-0.25}$	$9.40^{+2.31}_{-1.97}$	$1.28^{+0.24}_{-0.16}$	$3.17^{+0.99}_{-0.76}$	$1.90^{+0.22}_{-0.17}$	$0.81^{+0.99}_{-0.64}$
29	SOL2020-03-30T06:01	A1.8	$3.94^{+0.15}_{-0.11}$	$8.05^{+1.33}_{-1.49}$	$1.27^{+0.42}_{-0.28}$	$2.84^{+1.43}_{-1.08}$	$2.11^{+0.42}_{-0.30}$	$1.21^{+1.56}_{-0.90}$
30	SOL2020-03-30T10:40	A1.3	$4.21^{+0.17}_{-0.13}$	$6.54^{+1.15}_{-1.20}$	$1.07^{+0.64}_{-0.33}$	$2.34^{+1.90}_{-1.21}$	$1.77^{+0.57}_{-0.33}$	$1.10^{+1.52}_{-0.75}$
31	SOL2020-03-30T16:56	A1.9	$4.90^{+0.16}_{-0.15}$	$6.13^{+0.96}_{-0.88}$	$0.61^{+0.24}_{-0.17}$	$0.98^{+1.00}_{-0.82}$	$1.32^{+0.25}_{-0.20}$	$0.95^{+1.23}_{-0.70}$
32	SOL2020-03-30T18:28	A2.2	$5.05^{+0.28}_{-0.26}$	$5.93^{+1.60}_{-1.33}$	$1.13^{+0.23}_{-0.17}$	$2.73^{+0.95}_{-0.74}$	$2.00^{+0.24}_{-0.19}$	$0.87^{+1.05}_{-0.70}$
33	SOL2020-03-30T21:28	A1.0	$3.64^{+0.17}_{-0.13}$	$6.73^{+1.41}_{-1.48}$	$1.00^{+0.19}_{-0.15}$	$2.03^{+0.77}_{-0.63}$	$1.67^{+0.19}_{-0.16}$	$0.75^{+0.90}_{-0.61}$
34	SOL2020-03-31T08:09	A1.2	$3.52^{+0.09}_{-0.06}$	$11.11^{+1.11}_{-1.61}$	$0.98^{+0.19}_{-0.14}$	$2.74^{+0.86}_{-0.67}$	$1.78^{+0.20}_{-0.16}$	$0.88^{+1.03}_{-0.72}$
35	SOL2020-03-31T09:28	A1.5	$3.92^{+0.15}_{-0.11}$	$8.58^{+1.43}_{-1.60}$	$1.06^{+0.22}_{-0.15}$	$2.42^{+0.88}_{-0.67}$	$1.75^{+0.21}_{-0.16}$	$0.89^{+1.07}_{-0.72}$
36	SOL2020-03-31T13:01	A1.2	$4.03^{+0.30}_{-0.20}$	$6.05^{+1.69}_{-1.80}$	$1.28^{+0.23}_{-0.16}$	$3.73^{+1.02}_{-0.78}$	$2.07^{+0.23}_{-0.18}$	$0.82^{+0.99}_{-0.66}$
37	SOL2020-04-01T05:15	A1.3	$3.95^{+0.17}_{-0.12}$	$7.78^{+1.36}_{-1.53}$	$1.44^{+0.37}_{-0.25}$	$3.04^{+1.26}_{-0.95}$	$2.41^{+0.39}_{-0.29}$	$1.01^{+1.26}_{-0.78}$

Sl no	Flare ID	Flare Class (GOES approximation)	Temperature (MK)	Emission Measure ( $\times 10^{46} \text{cm}^{-3}$ )	Mg FIP bias	Al FIP bias	Si FIP bias	S FIP bias
38	SOL2020-04-01T07:47	A1.0	$3.99^{+0.22}_{-0.17}$	$5.30^{+1.26}_{-1.28}$	$1.01^{+0.27}_{-0.21}$	$1.80^{+0.93}_{-0.79}$	$1.75^{+0.29}_{-0.23}$	$1.16^{+1.42}_{-0.92}$
39	SOL2020-04-01T20:11	A1.7	$4.18^{+0.18}_{-0.13}$	$8.56^{+1.43}_{-1.63}$	$1.13^{+0.24}_{-0.19}$	$1.97^{+0.82}_{-0.70}$	$1.64^{+0.23}_{-0.19}$	$0.76^{+0.94}_{-0.60}$
40	SOL2020-04-02T02:04	A3.1	$4.95^{+0.16}_{-0.15}$	$9.27^{+1.50}_{-1.39}$	$0.97^{+0.16}_{-0.14}$	$2.09^{+0.64}_{-0.56}$	$1.41^{+0.15}_{-0.13}$	$0.73^{+0.84}_{-0.62}$
41	SOL2020-04-02T06:31	A1.2	$4.08^{+0.30}_{-0.22}$	$6.54^{+1.93}_{-1.90}$	$1.08^{+0.44}_{-0.30}$	$2.25^{+1.33}_{-1.06}$	$1.45^{+0.34}_{-0.24}$	$0.99^{+1.28}_{-0.74}$
42	SOL2020-04-02T07:32	A4.1	$5.29^{+0.16}_{-0.18}$	$12.65^{+2.06}_{-1.66}$	$0.93^{+0.38}_{-0.24}$	$1.51^{+1.22}_{-0.91}$	$1.68^{+0.36}_{-0.25}$	$1.27^{+1.63}_{-0.95}$
43	SOL2020-04-02T16:23	A1.6	$4.17^{+0.17}_{-0.14}$	$7.9^{+1.48}_{-1.54}$	$1.00^{+0.15}_{-0.11}$	$2.32^{+0.66}_{-0.52}$	$1.88^{+0.17}_{-0.13}$	$1.13^{+1.25}_{-1.02}$
44	SOL2020-04-04T03:09	A6.2	$5.60^{+0.29}_{-0.30}$	$18.05^{+4.60}_{-3.50}$	$0.97^{+0.45}_{-0.26}$	$1.95^{+1.52}_{-1.09}$	$1.51^{+0.38}_{-0.26}$	$0.89^{+1.28}_{-0.57}$
45	SOL2020-04-04T03:38	A2.0	$4.83^{+0.39}_{-0.38}$	$7.22^{+3.22}_{-2.28}$	$0.91^{+0.27}_{-0.20}$	$1.88^{+0.95}_{-0.78}$	$1.47^{+0.26}_{-0.20}$	$0.86^{+1.09}_{-0.66}$
46	SOL2020-04-04T06:03	A2.1	$4.49^{+0.42}_{-0.33}$	$8.88^{+3.63}_{-3.10}$	$0.33^{+0.21}_{-0.13}$	–	$0.82^{+0.19}_{-0.13}$	$0.81^{+1.03}_{-0.62}$
47	SOL2020-04-04T06:23	A4.5	$5.49^{+0.34}_{-0.33}$	$11.56^{+3.45}_{-2.74}$	$1.02^{+0.19}_{-0.16}$	$2.23^{+0.70}_{-0.65}$	$1.54^{+0.18}_{-0.16}$	$0.68^{+0.81}_{-0.56}$
48	SOL2020-04-04T07:02	A3.6	$5.25^{+0.22}_{-0.22}$	$9.9^{+2.10}_{-1.77}$	$0.64^{+0.20}_{-0.15}$	$0.86^{+0.72}_{-0.62}$	$1.25^{+0.19}_{-0.16}$	$0.88^{+1.08}_{-0.70}$
49	SOL2020-04-05T02:14	A1.1	$3.67^{+0.17}_{-0.15}$	$6.73^{+1.67}_{-1.46}$	$0.62^{+0.21}_{-0.16}$	$1.07^{+0.82}_{-0.68}$	$1.20^{+0.21}_{-0.17}$	$0.99^{+1.23}_{-0.78}$
50	SOL2020-04-05T07:42	A3.0	$5.06^{+0.19}_{-0.18}$	$9.01^{+1.68}_{-1.48}$	$0.97^{+0.29}_{-0.21}$	$2.20^{+1.06}_{-0.85}$	$1.75^{+0.31}_{-0.23}$	$0.95^{+1.20}_{-0.73}$
51	SOL2020-04-05T11:03	A1.8	$4.32^{+0.22}_{-0.18}$	$6.67^{+1.62}_{-1.60}$	$0.62^{+0.13}_{-0.11}$	$1.48^{+0.55}_{-0.50}$	$1.01^{+0.11}_{-0.10}$	$0.81^{+0.92}_{-0.70}$
52	SOL2020-04-06T03:57	A1.2	$3.68^{+0.25}_{-0.18}$	$8.08^{+2.20}_{-2.27}$	$0.99^{+0.22}_{-0.16}$	$1.92^{+0.78}_{-0.63}$	$1.99^{+0.26}_{-0.20}$	$1.02^{+1.29}_{-0.87}$
53	SOL2020-04-06T04:17	A1.4	$4.08^{+0.40}_{-0.28}$	$6.71^{+2.66}_{-2.48}$	$1.00^{+0.20}_{-0.16}$	$1.72^{+0.70}_{-0.61}$	$1.74^{+0.21}_{-0.18}$	$0.68^{+0.82}_{-0.56}$
54	SOL2020-04-06T13:23	A1.0	$3.44^{+0.19}_{-0.12}$	$8.80^{+1.81}_{-2.14}$	$1.04^{+0.18}_{-0.15}$	$2.25^{+0.68}_{-0.59}$	$1.79^{+0.19}_{-0.16}$	$1.06^{+1.19}_{-0.93}$
55	SOL2020-04-06T14:56	A1.0	$3.64^{+0.14}_{-0.09}$	$8.58^{+1.28}_{-1.66}$	$0.33^{+0.25}_{-0.17}$	–	$0.82^{+0.24}_{-0.17}$	$0.76^{+1.04}_{-0.54}$
56	SOL2020-04-06T18:36	A1.5	$4.42^{+0.30}_{-0.25}$	$5.82^{+1.89}_{-1.68}$	$0.74^{+0.17}_{-0.15}$	$0.97^{+0.62}_{-0.56}$	$1.47^{+0.19}_{-0.16}$	$0.87^{+1.03}_{-0.72}$
57	SOL2020-04-06T21:47	A6.9	$6.03^{+0.23}_{-0.24}$	$14.26^{+2.70}_{-2.22}$	$0.92^{+0.21}_{-0.17}$	$2.12^{+0.78}_{-0.67}$	$1.40^{+0.20}_{-0.16}$	$0.91^{+1.08}_{-0.76}$

Sl no	Flare ID	Flare Class (GOES approximation)	Temperature (MK)	Emission Measure ( $\times 10^{46} \text{cm}^{-3}$ )	Mg FIP bias	Al FIP bias	Si FIP bias	S FIP bias
58	SOL2020-04-07T08:29	A3.7	$5.81^{+0.27}_{-0.28}$	$8.26^{+2.01}_{-1.62}$	$0.87^{+0.25}_{-0.20}$	$1.70^{+0.81}_{-0.68}$	$1.60^{+0.26}_{-0.21}$	$1.10^{+1.30}_{-0.93}$
59	SOL2020-04-07T11:36	A1.1	$4.40^{+0.34}_{-0.29}$	$5.79^{+2.00}_{-1.70}$	$0.37^{+0.10}_{-0.10}$	$0.61^{+0.43}_{-0.44}$	$0.81^{+0.09}_{-0.09}$	$0.67^{+0.77}_{-0.58}$
60	SOL2020-04-07T12:58	A1.5	$4.76^{+0.51}_{-0.41}$	$5.01^{+2.47}_{-2.01}$	$0.36^{+0.09}_{-0.08}$	$0.60^{+0.44}_{-0.39}$	$0.84^{+0.09}_{-0.08}$	$0.68^{+0.78}_{-0.59}$
61	SOL2020-04-09T07:14	A2.0	$4.59^{+0.38}_{-0.31}$	$7.79^{+2.80}_{-2.45}$	$0.79^{+0.13}_{-0.12}$	$1.42^{+0.51}_{-0.50}$	$1.26^{+0.13}_{-0.12}$	$0.57^{+0.67}_{-0.49}$
62	SOL2020-04-10T00:22	A1.8	$4.99^{+0.24}_{-0.24}$	$5.42^{+1.39}_{-1.13}$	$0.75^{+0.27}_{-0.20}$	$1.36^{+0.92}_{-0.74}$	$1.30^{+0.26}_{-0.20}$	$0.77^{+0.99}_{-0.57}$
63	SOL2020-04-10T02:55	A2.0	$4.32^{+0.12}_{-0.09}$	$8.33^{+0.97}_{-1.14}$	$0.55^{+0.18}_{-0.15}$	$0.68^{+0.63}_{-0.58}$	$1.21^{+0.19}_{-0.16}$	$0.67^{+0.83}_{-0.53}$
64	SOL2020-04-10T22:40	A1.4	$4.68^{+0.17}_{-0.14}$	$5.36^{+0.85}_{-0.85}$	$0.66^{+0.09}_{-0.08}$	$1.42^{+0.37}_{-0.36}$	$1.05^{+0.08}_{-0.07}$	$0.56^{+0.61}_{-0.51}$
65	SOL2020-04-23T20:07	A1.5	$5.05^{+0.39}_{-0.35}$	$5.31^{+1.66}_{-1.38}$	$0.75^{+0.17}_{-0.15}$	$1.26^{+0.59}_{-0.53}$	$1.44^{+0.18}_{-0.16}$	$0.83^{+0.96}_{-0.71}$

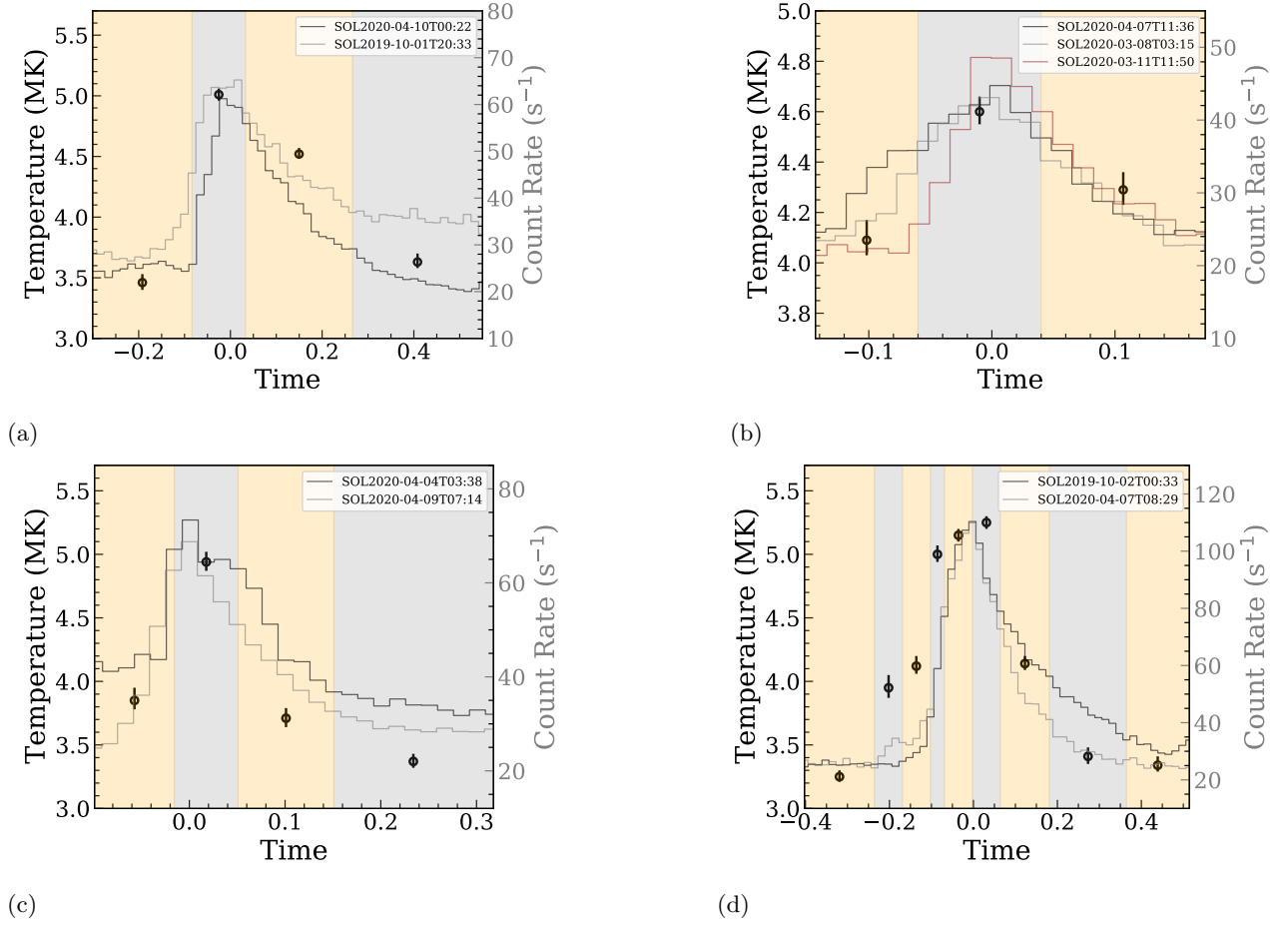


**Figure 9.** Evolution of temperature for the remaining sets of flares, similar to Figure 8 Panels a-c

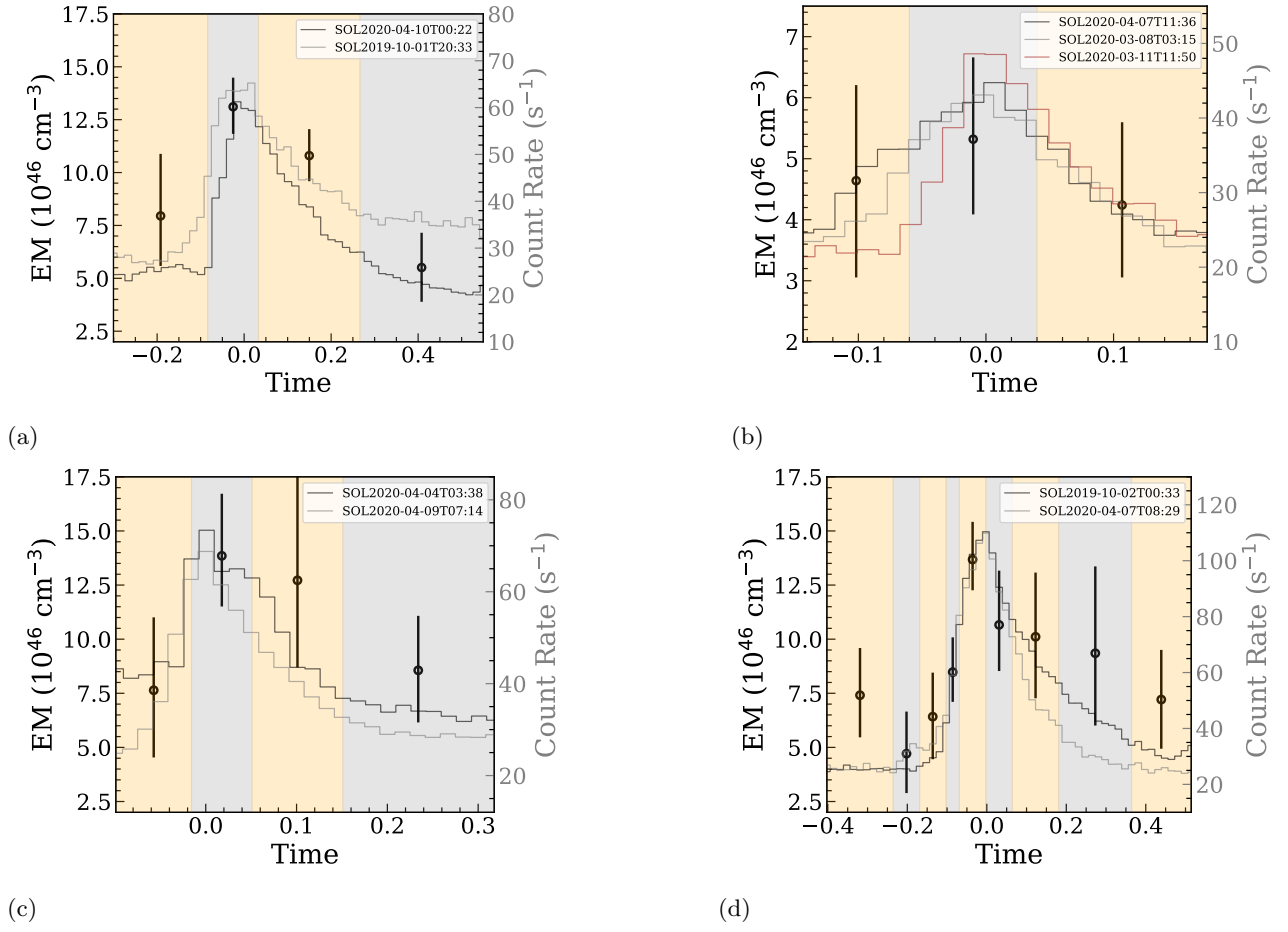


**Figure 10.** Evolution of emission measure for the remaining sets of flares, similar to Figure 7 Panels **d-f**



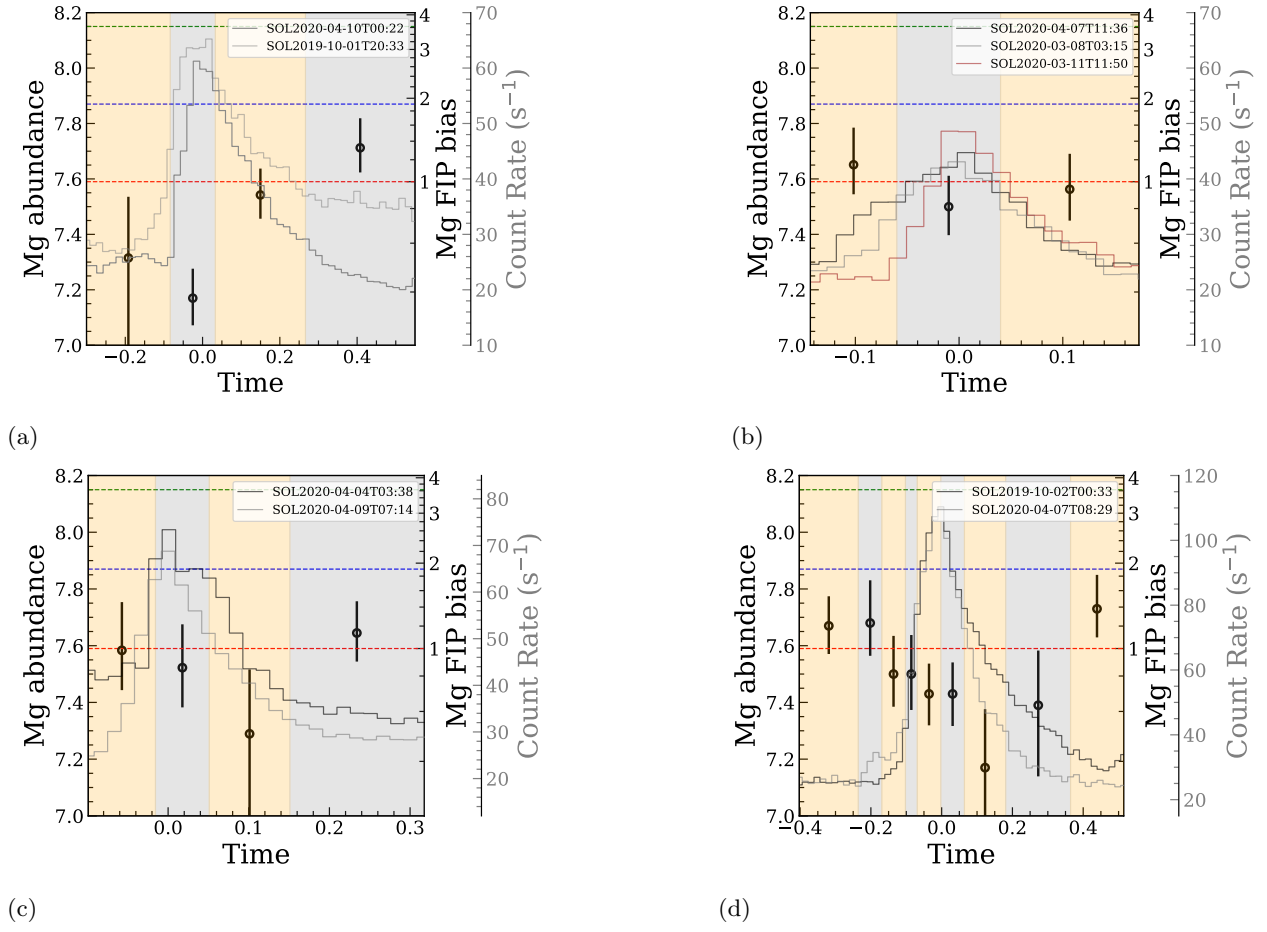


**Figure 11.** Evolution of absolute Magnesium abundance for the remaining sets of flares, similar to Figure 7 Panels **g-i**

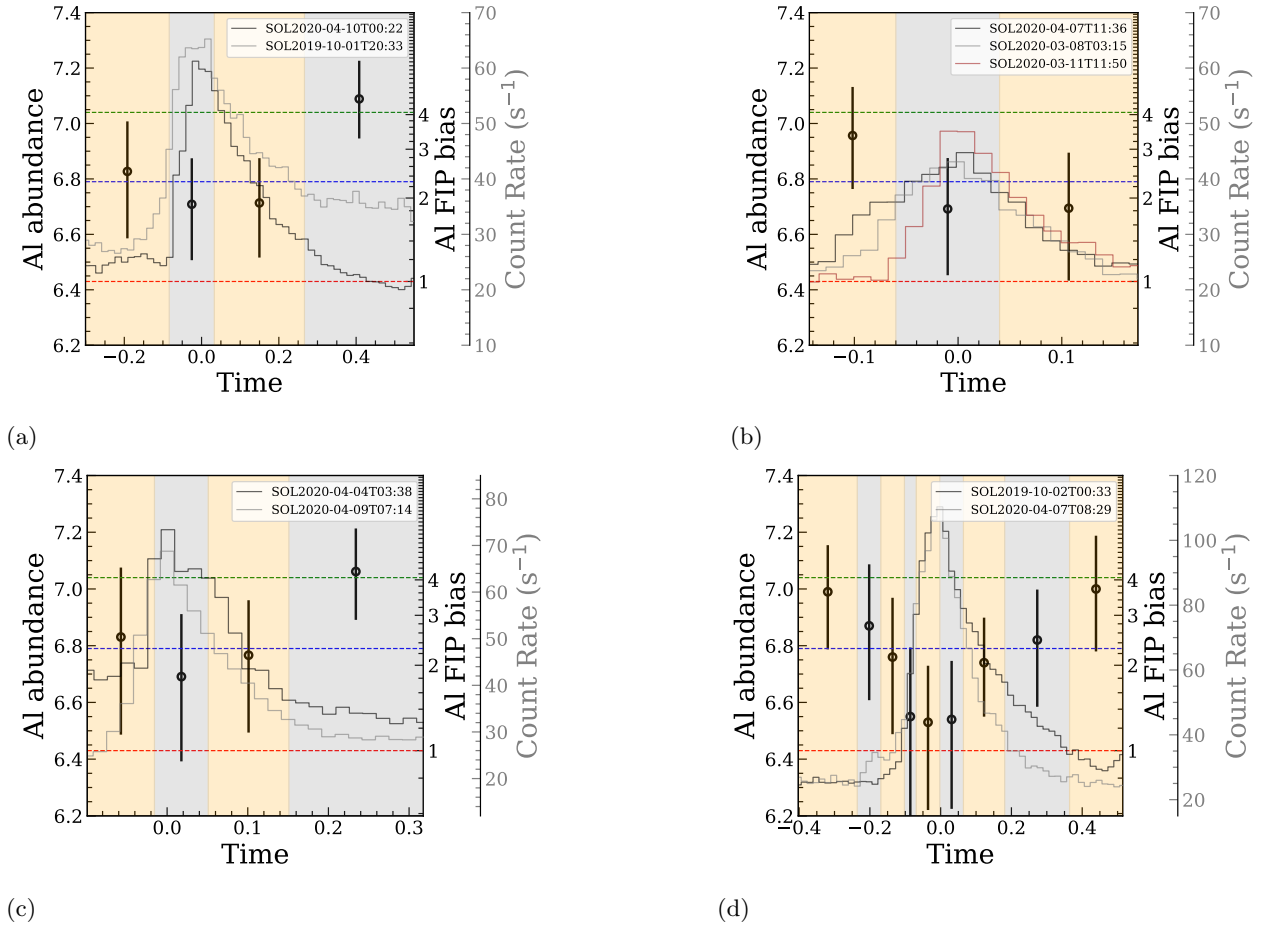


**Figure 12.** Evolution of absolute Aluminium abundance for the remaining sets of flares, similar to Figure 7 Panels j-l

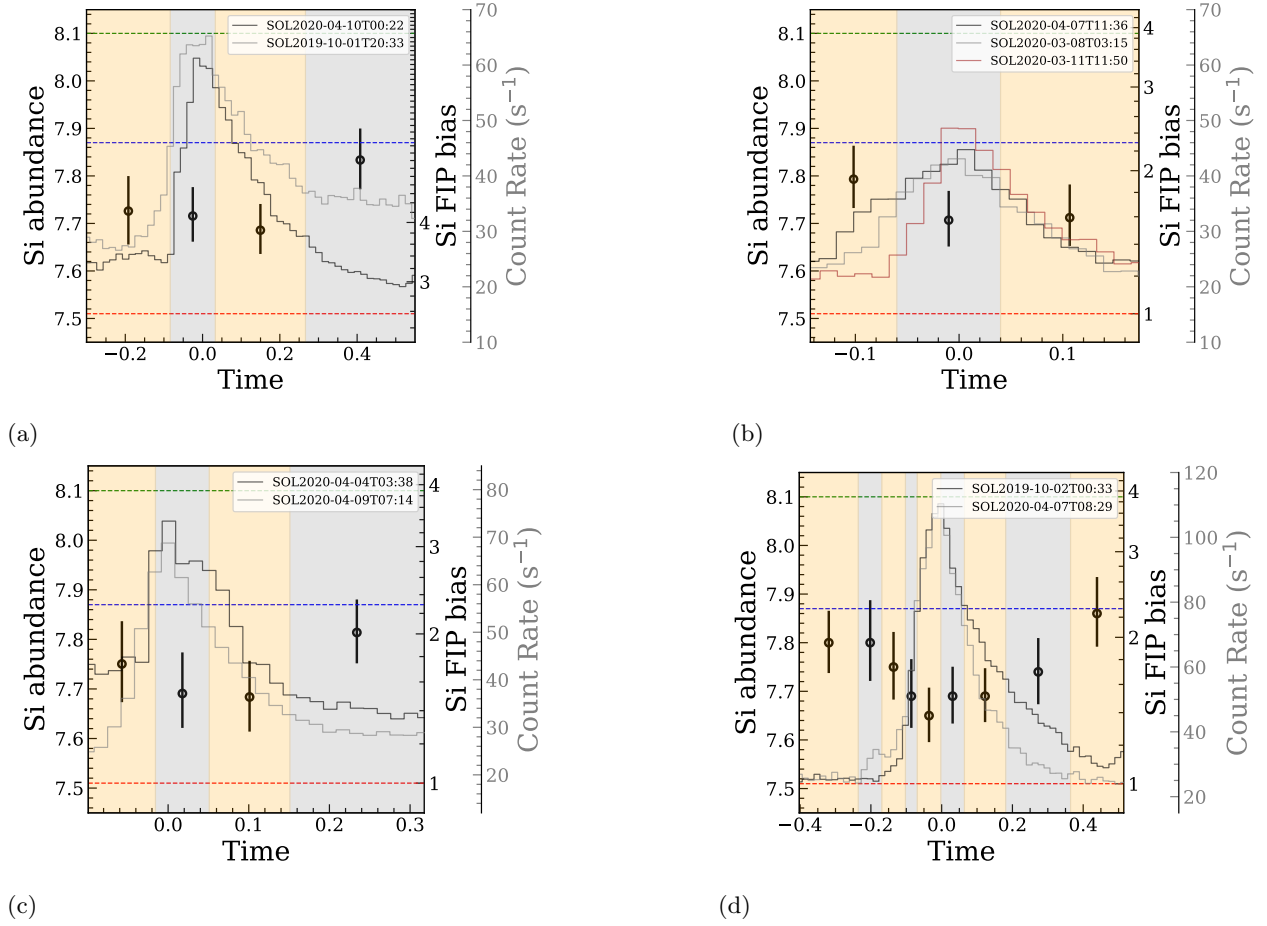


**Figure 13.** Evolution of absolute Silicon abundance for the remaining sets of flares, similar to Figure 7 Panels **m-o**

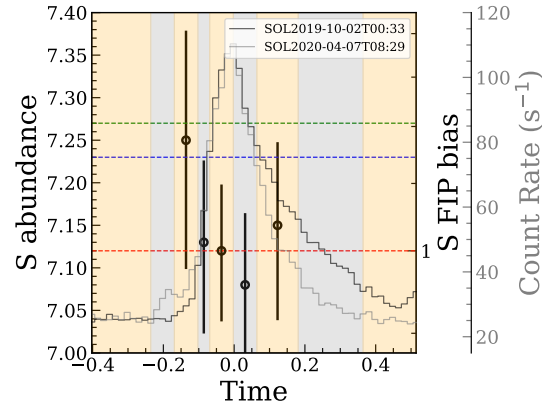


**Figure 14.** Evolution of absolute Sulfur abundance for the last set of flares, similar to Figure 7 Panel **p**

## References

- Antonucci, E., Dennis, B.R., Gabriel, A.H., Simnett, G.M.: 1985, Initial Phase of Chromospheric Evaporation in a Solar Flare. *Solar Phys.* **96**(1), 129. DOI. ADS.
- Arnaud, K., Dorman, B., Gordon, C.: 1999, *XSPEC: An X-ray spectral fitting package*. ADS.
- Asplund, M., Grevesse, N., Sauval, A.J., Scott, P.: 2009, The chemical composition of the sun. *Annual Review of Astronomy and Astrophysics* **47**(1), 481–522. DOI. <http://dx.doi.org/10.1146/annurev.astro.46.060407.145222>.
- Baker, D., Brooks, D.H., Démoulin, P., van Driel-Gesztelyi, L., Green, L.M., Steed, K., Carlyle, J.: 2013, Plasma Composition in a Sigmoidal Anemone Active Region. *Astrophys. J.* **778**(1), 69. DOI. ADS.
- Baker, D., Brooks, D.H., Démoulin, P., Yardley, S.L., van Driel-Gesztelyi, L., Long, D.M., Green, L.M.: 2015, FIP Bias Evolution in a Decaying Active Region. *Astrophys. J.* **802**(2), 104. DOI. ADS.
- Baker, D., van Driel-Gesztelyi, L., Brooks, D.H., Valori, G., James, A.W., Laming, J.M., Long, D.M., Démoulin, P., Green, L.M., Matthews, S.A., Oláh, K., Kővári, Z.: 2019, Transient Inverse-FIP Plasma Composition Evolution within a Solar Flare. *Astrophys. J.* **875**(1), 35. DOI. ADS.
- Benz, A.O.: 2017, Flare Observations. *Living Reviews in Solar Physics* **14**(1), 2. DOI. ADS.
- Bochsler, P.: 2007, Minor ions in the solar wind. *The Astronomy and Astrophysics Review* **14**, 1. DOI.
- Brooks, D.H., Baker, D., Van Driel-Gesztelyi, L., Warren, H.P.: 2017, A Solar cycle correlation of coronal element abundances in Sun-as-a-star observations. *Nature Communications* **8**(1). DOI.
- Carmichael, H.: 1964, A Process for Flares. In: *NASA Special Publication* **50**, 451. ADS.
- Culhane, J.L., Harra, L.K., James, A.M., Al-Janabi, K., Bradley, L.J., Chaudry, R.A., Rees, K., Tandy, J.A., Thomas, P., Whillock, M.C.R., Winter, B., Doschek, G.A., Korendyke, C.M., Brown, C.M., Myers, S., Mariska, J., Seely, J., Lang, J., Kent, B.J., Shaughnessy, B.M., Young, P.R., Simnett, G.M., Castelli, C.M., Mahmoud, S., Mapson-Menard, H., Probyn, B.J., Thomas, R.J., Davila, J., Dere, K., Windt, D., Shea, J., Hagood, R., Moye, R., Hara, H., Watanabe, T., Matsuzaki, K., Kosugi, T., Hansteen, V., Wikstol, Ø.: 2007, The EUV Imaging Spectrometer for Hinode. *Solar Phys.* **243**(1), 19. DOI. ADS.
- Dahlburg, R.B., Laming, J.M., Taylor, B.D., Obenschain, K.: 2016, Ponderomotive acceleration in coronal loops. *The Astrophysical Journal* **831**(2), 160. DOI. <https://dx.doi.org/10.3847/0004-637X/831/2/160>.
- Del Zanna, G., Mason, H.E.: 2018, Solar UV and X-ray spectral diagnostics. *Living Reviews in Solar Physics* **15**(1), 5. DOI. ADS.
- Del Zanna, G., Dere, K.P., Young, P.R., Landi, E.: 2021, CHIANTI—An Atomic Database for Emission Lines. XVI. Version 10, Further Extensions. *Astrophys. J.* **909**(1), 38. DOI. ADS.
- Dennis, B.R., Phillips, K.J.H., Schwartz, R.A., Tolbert, A.K., Starr, R.D., Nittler, L.R.: 2015, Solar flare element abundances from the solar assembly for x-rays (sax) onmesenger. *The Astrophysical Journal* **803**(2), 67. DOI. <http://dx.doi.org/10.1088/0004-637X/803/2/67>.
- Feldman, U.: 1992, Elemental abundances in the upper solar atmosphere. *Physica Scripta* **46**(3), 202. DOI. ADS.
- Feldman, U., Laming, J.: 2006, Element abundances in the upper atmospheres of the sun and stars: Update of observational results. *Physica Scripta* **61**, 222. DOI.
- Feldman, U., Widing, K.G.: 2003, Elemental abundances in the solar upper atmosphere derived by spectroscopic means. *Space Science Reviews* **107**, 665. DOI.
- Feldman, U., Widing, K.G.: 1990, Photospheric Abundances of Oxygen, Neon, and Argon Derived from the XUV Spectrum of an Impulsive Flare. *Astrophys. J.* **363**, 292. DOI. ADS.
- Feldman, U., Schühle, U., Widing, G., Laming, M.: 2009, Coronal composition above the solar equator and the north pole as determined from spectra acquired by the sumer instrument on soho. *The Astrophysical Journal* **505**, 999. DOI.
- Fludra, A., Schmelz, J.T.: 1999, The absolute coronal abundances of sulfur, calcium, and iron from Yokoh-BCS flare spectra. *Astron. Astrophys.* **348**, 286. ADS.
- Golub, L., Deluca, .E., Austin, .G., Bookbinder, .J., Caldwell, .D., Cheimets, .P., Cirtain, .J., Cosmo, .M., Reid, .P., Sette, .A., Weber, .M., Sakao, .T., Kano, .R., Shibasaki, .K., Hara, .H., Tsuneta, .S., Kumagai, .K., Tamura, .T., Shimojo, .M., Mccracken, .J., Carpenter, .J., Haight, .H., Siler, .R., Wright, .E., Tucker, .J., Rutledge, .H., Barbera, .M., Peres, .G., Varisco, .S., Deluca, E., Sakao, T., Kano, R., Shibasaki, K., Mccracken, J.: 2007, The X-Ray Telescope (XRT) for the Hinode Mission. *Solar Phys.* **243**, 63. DOI.
- Hefti, S., Fisk, L., Gloeckler, G., Von Steiger, R., Zurbuchen, T.: 1999, The transition between fast and slow solar wind from composition data. *Space Science Reviews* **87**. ISBN 978-90-481-5267-4. DOI.
- Hirayama, T.: 1974, Theoretical Model of Flares and Prominences. I: Evaporating Flare Model. *Solar Phys.* **34**(2), 323. DOI. ADS.
- Katsuda, S., Ohno, M., Mori, K., Beppu, T., Kanamaru, Y., Tashiro, M.S., Terada, Y., Sato, K., Morita, K., Sagara, H., Ogawa, F., Takahashi, H., Murakami, H., Nobukawa, M., Tsunemi, H., Hayashida, K., Matsumoto, H., Noda, H., Nakajima, H., Ezoe, Y., Tsuboi, Y., Maeda, Y., Yokoyama, T., Narukage, N.: 2020, Inverse First Ionization Potential Effects in Giant Solar Flares Found from Earth X-Ray Albedo with Suzaku/XIS. *Astrophys. J.* **891**(2), 126. DOI. ADS.
- Klimchuk, J.A.: 2017, Nanoflare Heating: Observations and Theory. *arXiv e-prints*, arXiv:1709.07320. ADS.
- Kopp, R.A., Pneuman, G.W.: 1976, Magnetic reconnection in the corona and the loop prominence phenomenon. *Solar Phys.* **50**(1), 85. DOI. ADS.
- Kosugi, T., Matsuzaki, K., Sakao, T., Shimizu, T., Sone, Y., Tachikawa, S., Hashimoto, T., Minesugi, K., Ohnishi, A., Yamada, T., Tsuneta, S., Hara, H., Ichimoto, K., Suematsu, Y., Shimojo, M., Watanabe, T., Shimada, S., Davis, J.M., Hill, L.D., Owens, J.K., Title, A.M., Culhane, J.L., Harra, L.K., Doschek, G.A., Golub, L.: 2007, The Hinode (Solar-B) Mission: An Overview. *Solar Phys.* **243**(1), 3. DOI. ADS.
- Laming, J.M.: 2004, A unified picture of the first ionization potential and inverse first ionization potential effects. *The Astrophysical Journal* **614**(2), 1063. DOI. <https://doi.org/10.1086/423780>.
- Laming, J.M.: 2012, Non-WKB Models of the First Ionization Potential Effect: The Role of Slow Mode Waves. *Astrophys. J.* **744**(2), 115. DOI. ADS.
- Laming, J.M.: 2015, The FIP and Inverse FIP Effects in Solar and Stellar Coronae. DOI. <http://arxiv.org/abs/1504.08325><http://dx.doi.org/10.1007/lrsp-2015-2>.
- Laming, J.M., Hwang, U.: 2009, Thermal conductivity and element fractionation in EV Lac. *Astrophysical Journal* **707**(1 PART 2), 60. DOI.
- Lemen, J.R., Title, A.M., Akin, D.J., Boerner, P.F., Chou, C., Drake, J.F., Duncan, D.W., Edwards, C.G., Friedlaender, F.M., Heyman, G.F., Hurlburt, N.E., Katz, N.L., Kushner, G.D., Levay, M., Lindgren, R.W., Mathur, D.P., McFeaters, E.L., Mitchell, S., Rehse, R.A., Schrijver, C.J., Springer, L.A., Stern, R.A., Tarbell, T.D., Wuelser, J.-P., Wolfson, C.J., Yanari, C., Bookbinder, J.A., Cheimets, P.N., Caldwell, D., Deluca, E.E., Gates, R., Golub, L., Park, S., Podgorski, W.A., Bush, R.I., Scherrer, P.H., Gumm, M.A., Smith, P., Auken, G., Jerram, P., Pool, P., Soufli, R., Windt, D.L., Beardsley, S., Clapp, M., Lang, J., Waltham, N.: 2012, The Atmospheric Imaging Assembly (AIA) on the Solar Dynamics Observatory (SDO). *Solar Phys.* **275**(1–2), 17. DOI. ADS.
- Meyer, J.-P.: 1985, Solar-stellar outer atmospheres and energetic particles, and galactic cosmic rays. *Astrophysical Journal Supplement* **57**, 173. DOI. ADS.

- Mithun, N.P.S., Vadawale, S.V., Sarkar, A., Shanmugam, M., Patel, A.R., Mondal, B., Joshi, B., Janardhan, P., Adalja, H.L., Goyal, S.K., et al.: 2020, Solar x-ray monitor on board the chandrayaan-2 orbiter: In-flight performance and science prospects. *Solar Physics* **295**(10). DOI: <http://dx.doi.org/10.1007/s11207-020-01712-1>.
- Mithun, N.P.S., Vadawale, S.V., Patel, A.R., Shanmugam, M., Chakrabarty, D., Konar, P., Sarvaiya, T.N., Padia, G.D., Sarkar, A., Kumar, P., et al.: 2021, Data processing software for chandrayaan-2 solar x-ray monitor. *Astronomy and Computing* **34**, 100449. DOI: <http://dx.doi.org/10.1016/j.ascom.2021.100449>.
- Mondal, B., Sarkar, A., Vadawale, S.V., Mithun, N.P.S., Janardhan, P., Zanna, G.D., Mason, H.E., Mitra-Kraev, U., Narendranath, S.: 2021, Evolution of elemental abundances during b-class solar flares: Soft x-ray spectral measurements with chandrayaan-2 XSM. *The Astrophysical Journal* **920**(1), 4. DOI: <https://doi.org/10.3847/1538-4357/ac14c1>.
- Munuswamy, S., Vadawale, S., Patel, A., Adalaja, H., N P S, M., Ladiya, T., Goyal, S., Tiwari, N., Singh, N., Kumar, S., Painkra, D., Acharya, Y., Bhardwaj, A., Hait, A., Patinge, A., Kapoor, A., Kumar, H., Satya, N.K., Saxena, G., Arvind, K.: 2020, Solar x-ray monitor onboard chandrayaan-2 orbiter. *Current Science* **118**, 45. DOI.
- N P S, M., Vadawale, S., Munuswamy, S., Patel, A., Tiwari, N., Adalja, H., Goyal, S., Ladiya, T., Singh, N., Kumar, S., Tiwari, M., Modi, M., Mondal, B., Sarkar, A., Joshi, B., Janardhan, P., Bhardwaj, A.: 2021, Ground calibration of solar x-ray monitor on board the chandrayaan-2 orbiter. *Experimental Astronomy* **51**, 1. DOI.
- Narendranath, S., Sreekumar, P., Alha, L., Sankarasubramanian, K., Huovelin, J., Athiray, P.S.: 2014, Elemental Abundances in the Solar Corona as Measured by the X-ray Solar Monitor Onboard Chandrayaan-1. *Solar Phys.* **289**(5), 1585. DOI. ADS.
- Narendranath, S., Sreekumar, P., Pillai, N.S., Panini, S., Sankarasubramanian, K., Huovelin, J.: 2020, Coronal elemental abundance: New results from soft x-ray spectroscopy of the sun. *Solar Physics* **295**(12). DOI: <http://dx.doi.org/10.1007/s11207-020-01738-5>.
- Pesnell, W.D., Thompson, B.J., Chamberlin, P.C.: 2012, The Solar Dynamics Observatory (SDO). *Solar Phys.* **275**(1-2), 3. DOI. ADS.
- Phillips, K.J.H., Dennis, B.R.: 2012, The Solar Flare Iron Abundance. *Astrophys. J.* **748**(1), 52. DOI. ADS.
- Phillips, K.J.H., Sylwester, J., Sylwester, B., Landi, E.: 2003, Solar Flare Abundances of Potassium, Argon, and Sulphur. *Astrophys. J. Lett.* **589**(2), L113. DOI. ADS.
- Pipin, V., Tomozov, V.: 2018, The nature of variations in anomalies of the chemical composition of the solar corona with the 11-year cycle. *Astronomy Reports* **62**, 281. DOI.
- Pottasch, S.R.: 1963, The Lower Solar Corona: Interpretation of the Ultraviolet Spectrum. *Astrophys. J.* **137**, 945. DOI. ADS.
- Ryan, D., Milligan, R., Gallagher, P., Dennis, B., Tolbert, A., Schwartz, R., Young, C.: 2012, The thermal properties of solar flares over three solar cycles using goes x-ray observations. *Astrophysical Journal Supplement Series* **202**, 11. DOI.
- Schmelz, J.T., Reames, D.V., von Steiger, R., Basu, S.: 2012, Composition of the Solar Corona, Solar Wind, and Solar Energetic Particles. *Astrophys. J.* **755**(1), 33. DOI. ADS.
- Sturrock, P.A.: 1966, Model of the High-Energy Phase of Solar Flares. *Nature* **211**(5050), 695. DOI. ADS.
- Sylwester, B., Sylwester, J., Phillips, K.J.H., Kepa, A., Mrozek, T.: 2014, Solar flare composition and thermodynamics from resik x-ray spectra. *The Astrophysical Journal* **787**(2), 122. DOI: <http://dx.doi.org/10.1088/0004-637X/787/2/122>.
- Sylwester, B., Phillips, K.J.H., Sylwester, J., Kepa, A.: 2015, Resik Solar X-Ray Flare Element Abundances on a Non-isothermal Assumption. *Astrophys. J.* **805**(1), 49. DOI. ADS.
- Sylwester, J., Lemen, J.R., Mewe, R.: 1984, Variation in observed coronal calcium abundance of X-ray flare plasmas. *Nature* **310**(5979), 665. DOI. ADS.
- Sylwester, J., Sylwester, B., Phillips, K.J.H., Kuznetsov, V.D.: 2012, The Solar Flare Sulfur Abundance from RESIK Observations. *Astrophys. J.* **751**(2), 103. DOI. ADS.
- Vadawale, S.V., Shanmugam, M., Acharya, Y.B., Patel, A.R., Goyal, S.K., Shah, B., Hait, A.K., Patinge, A., Subrahmanyam, D.: 2014, Solar X-ray Monitor (XSM) on-board Chandrayaan-2 orbiter. *Advances in Space Research* **54**(10), 2021. DOI. ADS.
- Vadawale, S.V., Mondal, B., Mithun, N.P.S., Sarkar, A., Janardhan, P., Joshi, B., Bhardwaj, A., Shanmugam, M., Patel, A.R., Adalja, H.K.L., et al.: 2021a, Observations of the quiet sun during the deepest solar minimum of the past century with chandrayaan-2 xsm: Elemental abundances in the quiescent corona. *The Astrophysical Journal Letters* **912**(1), L12. DOI: <http://dx.doi.org/10.3847/2041-8213/abf35d>.
- Vadawale, S.V., Mithun, N.P.S., Mondal, B., Sarkar, A., Janardhan, P., Joshi, B., Bhardwaj, A., Shanmugam, M., Patel, A.R., Adalja, H.K.L., et al.: 2021b, Observations of the quiet sun during the deepest solar minimum of the past century with chandrayaan-2 xsm: Sub-a-class microflares outside active regions. *The Astrophysical Journal Letters* **912**(1), L13. DOI: <http://dx.doi.org/10.3847/2041-8213/abf0b0>.
- Vanitha, M., Veeramuthuvel, P., Kalpana, K., Nagesh, G.: 2020, Chandrayaan-2: The Second Indian Mission to the Moon. In: *51st Annual Lunar and Planetary Science Conference, Lunar and Planetary Science Conference*, 1994. ADS.
- von Steiger, R., Schwadron, N.A., Fisk, L.A., Geiss, J., Gloeckler, G., Hefti, S., Wilken, B., Wimmer-Schweingruber, R.F., Zurbuchen, T.H.: 2000, Composition of quasi-stationary solar wind flows from Ulysses/Solar Wind Ion Composition Spectrometer. *J. Geophys. Res.* **105**(A12), 27217. DOI. ADS.
- Warren, H.P.: 2014, Measurements of Absolute Abundances in Solar Flares. *Astrophys. J. Lett.* **786**(1), L2. DOI. ADS.
- Widing, K.G., Feldman, U.: 2001, On the rate of abundance modifications versus time in active region plasmas. *The Astrophysical Journal* **555**(1), 426. DOI: <https://doi.org/10.1086/321482>.
- Zanna, G., Woods, T.: 2013, Spectral diagnostics with the sdo eve flare lines. *Astronomy and Astrophysics* **555**. DOI.
- Zanna, G.D., Mondal, B., Rao, Y.K., Mithun, N.P.S., Vadawale, S.V., Reeves, K.K., Mason, H.E., Sarkar, A., Janardhan, P., Bhardwaj, A.: 2022, Multiwavelength Observations by XSM, Hinode, and SDO of an Active Region. Chemical Abundances and Temperatures. *Astrophys. J.* **934**(2), 159. DOI. ADS.